PHYSICAL REVIEW B **96**, 174511 (2017)

Intrinsic ac anomalous Hall effect of nonsymmorphic chiral superconductors with an application to UPt$_3$

Zhiqiang Wang,[1] John Berlinsky,[1] Gertrud Zwicknagl,[2] and Catherine Kallin[1,3]
[1]*Department of Physics and Astronomy, McMaster University, Hamilton, Ontario, Canada L8S 4M1*
[2]*Institut für Mathematische Physik, Technische Universität Braunschweig, 38106 Braunschweig, Germany*
[3]*Canadian Institute for Advanced Research, Toronto, Ontario, Canada M5G 1Z8*

(Received 4 September 2017; published 16 November 2017)

We identify an intrinsic mechanism of the anomalous Hall effect for nonsymmorphic chiral superconductors. This mechanism relies on both a nontrivial multiband chiral superconducting order parameter, which is a mixture of pairings of even and odd angular momentum channels, and a complex normal-state intersublattice hopping, both of which are consequences of the nonsymmorphic group symmetry of the underlying lattice. We apply this mechanism to the putative chiral superconducting phase of the heavy-fermion superconductor UPt$_3$ and calculate the anomalous ac Hall conductivity in a simplified two-band model. From the ac Hall conductivity and optical data we estimate the polar Kerr rotation angle and compare it to the measured results for UPt$_3$ [Schemm *et al.*, Science **345**, 190 (2014)].

DOI: 10.1103/PhysRevB.96.174511

I. INTRODUCTION

Understanding unconventional superconductors has been one of the central goals in condensed matter research. Among the various unconventional superconductors, chiral superconductors have attracted a great deal of attention in recent years, in part because they provide a platform to study the interplay between spontaneous symmetry breaking and topology [1]. In a chiral superconductor, a Cooper pair carries a nonzero relative orbital angular momentum whose projection along a certain direction is also nonzero. Choosing this direction as the angular momentum quantization axis z, different chiral superconductors that are eigenstates of angular momentum can be characterized by the Cooper-pair orbital angular momentum quantum numbers $L = 1,2,3,\ldots$ and $L_z = \pm 1,\pm 2,\ldots$. A general chiral superconducting order, however, need not be an angular momentum eigenstate. For example, chiral f wave may mix with chiral p wave, etc.

One of the defining properties of a chiral superconductor is its spontaneous breaking of parity and time-reversal symmetry. As a consequence, there can be a nonzero anomalous Hall effect (i.e., a Hall effect in the absence of an external magnetic field), which can be detected by polar Kerr effect measurements [2]. Experimentally, a frequency-dependent rotation angle between the polarization of incident and reflected light is measured. This Kerr angle $\theta_K(\omega)$ is related to the ac anomalous Hall conductivity $\sigma_H(\omega)$ by [3]

$$\theta_K(\omega) = \frac{4\pi}{\omega}\,\mathrm{Im}\left[\frac{\sigma_H(\omega)}{n(n^2-1)}\right], \tag{1}$$

where n is the frequency-dependent index of refraction. A nonzero Kerr signal has been observed in the superconducting phase of several unconventional superconductors including Sr$_2$RuO$_4$ [4], UPt$_3$ [5], URu$_2$Si$_2$ [6], PrOs$_4$Sb$_{12}$ [7], and Bi/Ni bilayers [8]. Sr$_2$RuO$_4$ is widely thought to be a chiral p-wave superconductor [9,10], while the heavy-fermion superconductor UPt$_3$ is expected to be a chiral f-wave superconductor with E_{2u} symmetry, corresponding to $L = 3$, $L_z = \pm 2$ in the continuum limit [11,12].

However, parity and time-reversal symmetry breaking are necessary but not sufficient conditions for a nonzero anomalous Hall effect. Breaking of additional symmetries, translation and particle hole, are needed for a nonzero $\sigma_H(\omega)$. Consequently, the size of the effect depends crucially on the mechanism by which these symmetries are broken. As pointed out previously [13–15], $\sigma_H(\omega)$ vanishes at all frequencies for a Galliean invariant chiral superconductor. One way to break translation symmetry is by extrinsic impurity scattering, which has been studied by several groups in the context of Sr$_2$RuO$_4$ [15–17]. This impurity effect does not contribute to σ_H in the lowest-order Born approximation and therefore requires higher-order scattering [16]. However, both Sr$_2$RuO$_4$ and UPt$_3$ are very clean, and it is not clear if the observed effect is due to disorder. Even without impurities, translation symmetry can be broken by certain intrinsic mechanisms, which turn out to be rather subtle. There have been two intrinsic mechanisms proposed previously. One is based on a collective mode [18], combined with the small but finite momentum of the incident photon and the breaking of inversion symmetry along the incident external electromagnetic wave propagation direction. However, the estimated angle for this mechanism is too small to account for experiments [4]. The other intrinsic mechanism invokes a multiband effect [19–23], arising from structure within the crystal unit cell, which also involves interband pairing. Here, we will study a generalization of this multiband mechanism.

All of these theories (impurity effects, collective modes, and the multiband effect) have so far only been studied for the case of chiral p-wave superconductors. This has led to a better understanding of the Kerr effect in Sr$_2$RuO$_4$. However, UPt$_3$ is thought to be a chiral f-wave superconductor in its lower superconducting transition temperature phase. One might think that the conclusions obtained for the Kerr effect in a chiral p-wave superconductor can be directly generalized to higher-chirality superconductors with $|L_z| \geqslant 2$ without much difficulty. However, such a naive generalization is problematic. As recent studies on nontopologically protected quantities, such as the integrated edge current [24] and the total orbital angular momentum [25,26], have demonstrated

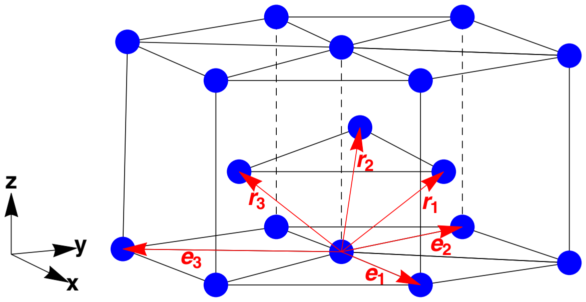

FIG. 1. Crystal structure of UPt$_3$. Blue disks denote the positions of U atoms. There is a Pt atom (not shown) between each nearest-neighbor intralayer pair of U atoms. The vectors $\mathbf{e}_i$ and $\mathbf{r}_i$ connect two nearest-neighbor intralayer and interlayer U atoms, respectively. The coordinate system is chosen such that $\hat{x} \parallel \mathbf{e}_1$.

explicitly, chiral superconductors with $|L_z| \geqslant 2$ can behave very differently from the chiral p-wave case. Given that the anomalous Hall conductivity $\sigma_H(\omega)$ is also a nontopologically protected quantity [13,15], unlike its thermal Hall counterpart, we expect that $\sigma_H(\omega)$ of chiral superconductors with $|L_z| \geqslant 2$ can be quite different from that of $|L_z| = 1$. In fact, as has already been pointed out by Goryo in Ref. [16], in the continuum limit, the skew impurity scattering diagram for the lowest-order impurity contribution to $\sigma_H(\omega)$ is nonzero only for chiral superconductors with $|L_z| = 1$ and vanishes for $|L_z| \geqslant 2$. More generally, to have a nonzero σ_H in the continuum limit, the azimuthal angular integral of $k_x k_y \Delta_1 \Delta_2^*$, where $\Delta_{1,2}$ are the two components of the chiral order parameter, must be nonzero. While the details differ somewhat for the different mechanisms, the $k_x k_y$ in the angular integral effectively arises from the current (or velocity) operators in σ_{xy} and $\Delta_1 \Delta_2^*$ is the lowest-order contribution that directly brings in the chirality to which σ_H is proportional. It follows that $\sigma_H \neq 0$ only for $|L_z| = 1$. The vanishing of σ_H for higher-chirality superconductors in the continuum limit is a concern for UPt$_3$ because the observed Kerr signal in UPt$_3$ [5] is actually larger than in Sr$_2$RuO$_4$ [4]. To get a nonzero anomalous Hall conductivity for UPt$_3$ from chiral f-wave order, one needs to include lattice or band-structure effects.

UPt$_3$ exhibits multiple superconducting phases in its temperature magnetic field phase diagram [27–29]. At zero field it undergoes two separate superconducting transitions at $T_c^+ \approx 0.55$ K and $T_c^- \approx 0.5$ K [30–34]. A nonzero Kerr rotation [5] has been observed only in the superconducting phase below T_c^-. To study whether this UPt$_3$ Kerr effect can arise from the multiband mechanism, one needs a model with at least two bands. The simplest case is two bands arising from the ABAB stacking of the hexagonal planes of the U atoms along the crystal c axis. (See Fig. 1.) Due to this stacking, the crystal has a close-packed hexagonal lattice structure corresponding to the nonsymmorphic space group $P6_3/mmc$. One can ask if the two bands resulting from this stacking can give rise to a nonzero Kerr effect. In fact, as will be discussed later, one can show that a simple chiral d- or f-wave pairing on a triangular lattice with ABAB stacking gives zero, even including lattice effects beyond the continuum limit.

Recently, Yanase [35] argued that, due to the nonsymmorphic space group, the spin triplet superconducting order parameter is not a simple chiral f wave or a combination of only f and p waves. Chiral d-wave pairing also mixes with the symmetry of the E_{2u} representation of the crystal lattice point group D_{6h}. In this model, chiral f and p waves are even in the sublattice index, which can be thought of as an extra pseudospin index, while chiral d wave is odd in that index and, consequently, chiral f pairing is a triplet in the AB-sublattice subspace while the chiral d-wave pairing is a singlet. Both f and d components involve nearest-neighbor interlayer pairing and are of the same magnitude, while the chiral p-wave component involves pairing within the basal plane and is expected to be smaller. The smaller p-wave pairing amplitude is presumably conjectured because of the relatively larger in-plane U-U atom distance [36] and perhaps also because the chiral p component is energetically unfavorable since it pairs only one spin component. The mixing of chiral f and d waves leads to a more complex chiral $f + d$ pairing order parameter that is nonunitary [35].

As a simple model, following Yanase, we study the two bands, resulting from the ABAB stacking, that model the "starfishlike" Fermi surfaces [30,37], centered on the A point at the top and bottom of the Brillouin zone (BZ). There are also four other Fermi surface sheets resolved experimentally [30,37], which, however, will not be considered in this paper. The four other Fermi sheets are not simply related by stacking since, in general, the two bands due to the stacking (the bonding and antibonding bands) are well separated in energy and only one of them crosses the Fermi energy. However, in the case of the "starfish" Fermi surfaces on the BZ boundary, without spin-orbit coupling (SOC) the two bands are degenerate by symmetry on the top and bottom BZ faces. With SOC, band degeneracies remain along six directions on the top and bottom surfaces. These bands give a particularly simple two-band model for studying the intrinsic multiband mechanism of the Kerr effect.

In this paper, we show that this two-band model with a mixed $(f + d)$-wave superconducting order parameter can give rise to a nonzero Kerr effect with or without the small chiral p-wave pairing component. We find that mixing of the chiral d component with the chiral f-wave pairing is essential for a nonzero σ_H. We also find that the nature of the terms that contribute to σ_H are distinct from the terms that give a nonzero contribution for the Sr$_2$RuO$_4$ case [19]. From σ_H we estimate the Kerr angle and find it to be about 10% of the experimental value in UPt$_3$ [5]. Factors that might increase (or decrease) this estimate are discussed.

Although our work is not a complete theory of the Kerr effect for UPt$_3$, it captures a key possible contribution and more generally illustrates the necessary ingredients for a nonzero Kerr effect for a higher chirality superconductor, a case which is noticeably more subtle than that of chiral p wave.

The paper is organized as follows. In Sec. II we describe the Bogoliubov–de Gennes (BdG) Hamiltonian that we use for the starfishlike Fermi surface. In Sec. III we derive an approximate expression for $\sigma_H(\omega)$ for this BdG Hamiltonian, evaluate it numerically, and identify the key ingredients of the result. The estimation of the Kerr angle from σ_H and comparison to experiment are given in Sec. IV. Section V contains our conclusions and further discussions. Some technical computational details are relegated to the Appendices.

II. MODEL

We focus on a two-band model proposed by Yanase [35] to describe the starfish Fermi surface (FS) of $\mathrm{UPt_3}$. With the two sublattices and two spin components, the BdG Hamiltonian can be written in terms of an eight-component spinor $\Psi(k)$ whose transpose is defined as

$$\Psi_{\mathbf{k}}^{T} \equiv (c_{\mathbf{k}1\uparrow},c_{\mathbf{k}2\uparrow},c_{\mathbf{k}1\downarrow},c_{\mathbf{k}2\downarrow},c^{\dagger}_{-\mathbf{k}1\uparrow},c^{\dagger}_{-\mathbf{k}2\uparrow},c^{\dagger}_{-\mathbf{k}1\downarrow},c^{\dagger}_{-\mathbf{k}2\downarrow}), \tag{2}$$

where $c_{\mathbf{k}is}$ is the annihilation operator for an electron with momentum $\mathbf{k}$, sublattice index i, and spin quantum number s. In this basis, the BdG Hamiltonian can be written as

$$\mathcal{H}_{\mathrm{BdG}} = \frac{1}{2}\sum_{\mathbf{k}\in\mathrm{BZ}} \Psi_{\mathbf{k}}^{\dagger}\hat{\mathcal{H}}_{\mathrm{BdG}}(\mathbf{k})\Psi_{\mathbf{k}}, \tag{3}$$

with

$$\hat{\mathcal{H}}_{\mathrm{BdG}}(\mathbf{k}) = \begin{pmatrix} \hat{\mathcal{E}}(\mathbf{k}) & \hat{\Delta}(\mathbf{k}) \\ \hat{\Delta}^{\dagger}(\mathbf{k}) & -\hat{\mathcal{E}}^{T}(-\mathbf{k}) \end{pmatrix}, \tag{4}$$

where $\hat{\mathcal{E}}(\mathbf{k})$ is the normal-state Hamiltonian and $\hat{\Delta}_{\mathbf{k}}$ is the superconducting order parameter, both 4×4 matrices.

A. Normal-state Hamiltonian and Fermi surfaces

Using σ_α and s_α to denote the four Pauli matrices for the two sublattices and spin, respectively, we can write the normal-state Hamiltonian $\hat{\mathcal{E}}(\mathbf{k})$ as

$$\hat{\mathcal{E}}(\mathbf{k}) = \xi_{\mathbf{k}}\sigma_0 s_0 + \frac{\epsilon_{\mathbf{k}}}{\sqrt{2}}\,\sigma_+ s_0 + \frac{\epsilon_{\mathbf{k}}^{*}}{\sqrt{2}}\,\sigma_- s_0 + \mathbf{g}_{\mathbf{k}}\cdot\mathbf{s}\,\sigma_3, \tag{5}$$

where $\sigma_\pm = (\sigma_1 \pm i\sigma_2)/\sqrt{2}$ and $\xi_{\mathbf{k}}$, $\epsilon_{\mathbf{k}}$, and $\mathbf{g}_{\mathbf{k}}$ are given by

$$\xi_{\mathbf{k}} = 2t\sum_{i=1}^{3}\cos\mathbf{k}_{\parallel}\cdot\mathbf{e}_i + 2t_z\cos k_z - \mu, \tag{6a}$$

$$\epsilon_{\mathbf{k}} = 2t'\cos\frac{k_z}{2}\sum_{i=1}^{3}e^{i\mathbf{k}_{\parallel}\cdot\mathbf{r}_i}, \tag{6b}$$

$$\mathbf{g}_{\mathbf{k}} = \hat{z}\,\alpha\sum_{i=1}^{3}\sin\mathbf{k}_{\parallel}\cdot\mathbf{e}_i. \tag{6c}$$

Here, $\xi_{\mathbf{k}}$ contains all nearest-neighbor (NN) hoppings within the same sublattice, both in-plane hopping with parameter t and intrasublattice NN hopping along the c axis with parameter t_z, μ is the chemical potential and $\mathbf{k}_{\parallel} = (k_x,k_y,0)$. The three unit vectors $\mathbf{e}_i = (\cos\phi_i,\sin\phi_i,0)$ with $\phi_i = (i-1)\frac{2\pi}{3}$ and $i = \{1,2,3\}$, are defined within the plane as shown in Fig. 1. (All lattice spacings are set to unity.) $\epsilon_{\mathbf{k}}$ describes intersublattice NN hopping with parameter t'. The prefactor $\cos\frac{k_z}{2}$ in $\epsilon_{\mathbf{k}}$ comes from the fact that these hoppings are defined on the intersublattice bonds which are described by three nonprimitive lattice vectors: $\mathbf{r}_i = (\frac{1}{\sqrt{3}}\cos\phi_i', \frac{1}{\sqrt{3}}\sin\phi_i', \frac{1}{2})$, with $\phi_i' = \frac{\pi}{6} + (i-1)\frac{2\pi}{3}$. $\mathbf{g}_k\cdot\mathbf{s}$ is a Kane-Mele–type spin-orbit coupling (SOC) [38,39] that is allowed since the local symmetry of each U atom is D_{3h}, which does not have inversion. Note this SOC term cannot exist between two different sublattices because the center of the intersublattice U-U bond is inversion symmetric. Also, the SOCs for the two sublattices must have opposite signs in order for the U lattice to restore its global D_{6h} symmetry which preserves inversion [35]. This explains the presence of the Pauli matrix σ_3 in the SOC term in the expression of $\hat{\mathcal{E}}(\mathbf{k})$. The parameter α in $\mathbf{g}_{\mathbf{k}}$ characterizes the SOC strength.

Diagonalizing the Hamiltonian $\hat{\mathcal{E}}(\mathbf{k})$ gives the two normal-state band dispersions $E_{\pm}^{(n)}(\mathbf{k}) = \xi_{\mathbf{k}} \pm \sqrt{g_{\mathbf{k}}^2 + |\epsilon_{\mathbf{k}}|^2}$, each of which is twofold degenerate. The Fermi surfaces are shown in Fig. 2 for the parameters $(t,t_z,t',\alpha,\mu) = (1,-4,1,2,12)$ from Ref. [35]. Figure 2(a) shows that the FS is centered around the A point of the BZ, while Fig. 2(b) presents a cut of the FS on the zone boundary $k_z = \pi$ plane. Note, from Fig. 2(b), the two Fermi surfaces intersect at six points on that plane since $\epsilon_{\mathbf{k}} = 0$ for $k_z = \pi$ and $g_{\mathbf{k}}$ vanishes along the sixfold-symmetric directions: $k_y/k_x = \tan\theta_i$ with $\theta_i = \frac{\pi}{6} + (i-1)\frac{\pi}{3}$.

B. Superconducting order parameter $\hat{\Delta}(\mathbf{k})$

The superconducting order parameter $\hat{\Delta}(\mathbf{k})$ proposed in Ref. [35] is an E_{2u} state that can be written as $\hat{\Delta}(\mathbf{k}) = \eta_1\hat{\Gamma}_1(\mathbf{k}) + \eta_2\hat{\Gamma}_2(\mathbf{k})$. Here, $\hat{\Gamma}_1(\mathbf{k})$ and $\hat{\Gamma}_2(\mathbf{k})$ are two basis functions of the E_{2u} representation, and $(\eta_1,\eta_2) = \Delta_0(1,i\eta)/\sqrt{1+\eta^2}$, with overall pairing magnitude Δ_0 and η a real number that controls the anisotropy of the order parameter. Due to the relative phase between η_1 and η_2, $\hat{\Delta}(\mathbf{k})$ is chiral, with the chirality determined by the sign of η.

$\hat{\Gamma}_1(\mathbf{k})$ and $\hat{\Gamma}_2(\mathbf{k})$ are both triplets in spin as suggested by experiments [11,30,40]. The spatial parts of $\hat{\Gamma}_1(\mathbf{k})$ and $\hat{\Gamma}_2(\mathbf{k})$ contain not only f- and p-wave components but also a d-wave component as discussed above. Spatial inversion operation not only transforms $\mathbf{k}\to-\mathbf{k}$ but also interchanges the two sublattices. The f- and p-wave components are odd functions of $\mathbf{k}$ and triplets in the sublattice index, while the d component is an even function of $\mathbf{k}$ but a sublattice singlet. As mentioned above, the pairing amplitudes of the f- and d-wave components connect different sublattices while the p-wave component pairs sites on the same sublattice. The f and d components are of similar magnitude while the p wave is smaller. In the following, we will ignore this small p component. Then, the two basis functions $\hat{\Gamma}_1$ and $\hat{\Gamma}_2$ can be written as [35]

$$\hat{\Gamma}_1(\mathbf{k}) = \{f_{(x^2-y^2)z}(\mathbf{k})\sigma_1 - d_{yz}(\mathbf{k})\sigma_2\}s_1, \tag{7a}$$

$$\hat{\Gamma}_2(\mathbf{k}) = \{f_{xyz}(\mathbf{k})\sigma_1 - d_{xz}(\mathbf{k})\sigma_2\}s_1, \tag{7b}$$

where, for nearest-neighbor intersublattice pairing,

$$f_{(x^2-y^2)z}(\mathbf{k}) = -\sin\frac{k_z}{2}\left[\cos\frac{k_x}{2}\cos\frac{k_y}{2\sqrt{3}} - \cos\frac{k_y}{\sqrt{3}}\right], \tag{8a}$$

$$f_{xyz}(\mathbf{k}) = \sqrt{3}\sin\frac{k_x}{2}\sin\frac{k_y}{2\sqrt{3}}\sin\frac{k_z}{2}, \tag{8b}$$

$$d_{yz}(\mathbf{k}) = -\sin\frac{k_z}{2}\left[\cos\frac{k_x}{2}\sin\frac{k_y}{2\sqrt{3}} + \sin\frac{k_y}{\sqrt{3}}\right], \tag{8c}$$

$$d_{xz}(\mathbf{k}) = -\sqrt{3}\sin\frac{k_x}{2}\cos\frac{k_y}{2\sqrt{3}}\sin\frac{k_z}{2}. \tag{8d}$$

In the expressions for $\hat{\Gamma}_1(\mathbf{k})$ and $\hat{\Gamma}_2(\mathbf{k})$, the spin Pauli matrix $s_1 = s_3\,i s_2$ indicates that the spin triplet pairing $\mathbf{d}$ vector is

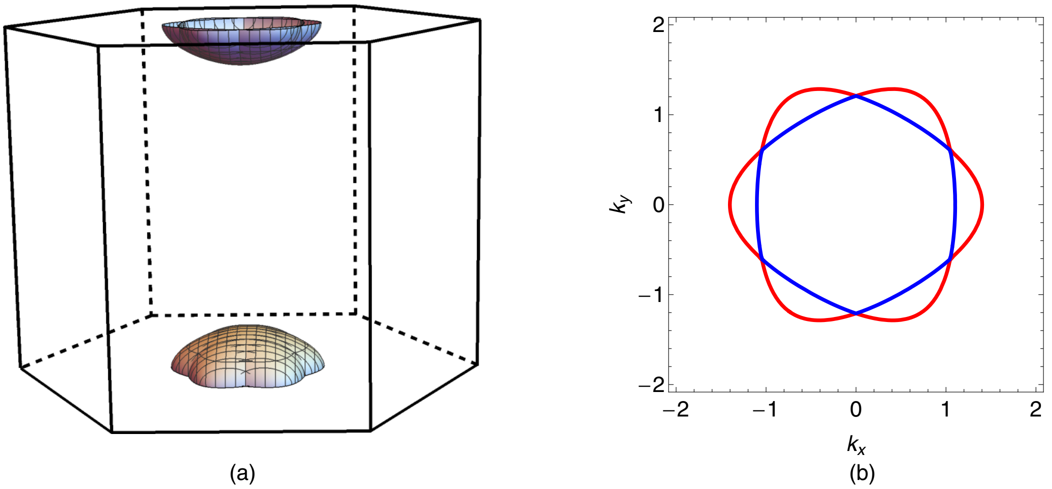

FIG. 2. Starfish Fermi surface (FS). (a) FS in the three-dimensional Brillouin zone of UPt$_3$; (b) FS contours in the plane of $k_z = \pi$. The red (blue) line is the $E_+^{(n)}(\mathbf{k}) = 0$ [$E_-^{(n)}(\mathbf{k}) = 0$] constant energy contour. Parameters used are $(t,t_z,t',\alpha,\mu) = (1,-4,1,2,12)$.

along the $\hat{z}$ direction (or the crystal c axis). The presence of sublattice Pauli matrices σ_1 and σ_2 comes from the fact that the f- and d-wave components are derived from the real and imaginary parts, respectively, of a pairing amplitude for electrons from NN intersublattice U ions. Because of the mixing between the f- and d-wave components,

$$\hat{\Delta}(\mathbf{k})\hat{\Delta}^\dagger(\mathbf{k}) = \{|f_\mathbf{k}|^2 + |d_\mathbf{k}|^2\}\sigma_0 s_0 - i\{f_\mathbf{k} d^*_\mathbf{k} - f^*_\mathbf{k} d_\mathbf{k}\}\sigma_3 s_0 \tag{9}$$

has a term which is not proportional to the identity matrix $\sigma_0 s_0$, which makes $\hat{\Delta}(\mathbf{k})$ nonunitary [41]. In Eq. (9),

$$f_\mathbf{k} \equiv \eta_1 f_{(x^2-y^2)z}(\mathbf{k}) + \eta_2 f_{xyz}(\mathbf{k}), \tag{10a}$$

$$d_\mathbf{k} \equiv \eta_1 d_{yz}(\mathbf{k}) + \eta_2\, d_{xz}(\mathbf{k}). \tag{10b}$$

C. Reduction of the BdG Hamiltonian

The expressions for $\hat{\mathcal{E}}(\mathbf{k})$ and $\hat{\Delta}(\mathbf{k})$ defined above can now be substituted into the BdG Hamiltonian given by Eq. (4). One finds $\mathcal{H}_{\rm BdG}(\mathbf{k})$ reduces to two decoupled 4×4 blocks:

$$\begin{aligned}\mathcal{H}_{\rm BdG} &= \mathcal{H}^{(a)} + \mathcal{H}^{(b)}\\ &= \frac{1}{2}\sum_{i=a,b}\sum_{\mathbf{k}\in {\rm BZ}}\big[\Psi^{(i)}_\mathbf{k}\big]^\dagger \hat{\mathcal{H}}^{(i)}(\mathbf{k})\Psi^{(i)}_\mathbf{k},\end{aligned} \tag{11}$$

with

$$\hat{\mathcal{H}}^{(a)} = \begin{pmatrix} \xi_\mathbf{k} + g_\mathbf{k} & \epsilon_\mathbf{k} & 0 & \Delta_{12}(\mathbf{k}) \\ \epsilon^*_\mathbf{k} & \xi_\mathbf{k} - g_\mathbf{k} & \Delta_{21}(\mathbf{k}) & 0 \\ 0 & \Delta^*_{21}(\mathbf{k}) & -\xi_\mathbf{k} - g_\mathbf{k} & -\epsilon_\mathbf{k} \\ \Delta^*_{12}(\mathbf{k}) & 0 & -\epsilon^*_\mathbf{k} & -\xi_\mathbf{k} + g_\mathbf{k} \end{pmatrix}, \tag{12a}$$

$$\hat{\mathcal{H}}^{(b)} = \begin{pmatrix} \xi_\mathbf{k} - g_\mathbf{k} & \epsilon_\mathbf{k} & 0 & \Delta_{12}(\mathbf{k}) \\ \epsilon^*_\mathbf{k} & \xi_\mathbf{k} + g_\mathbf{k} & \Delta_{21}(\mathbf{k}) & 0 \\ 0 & \Delta^*_{21}(\mathbf{k}) & -\xi_\mathbf{k} + g_\mathbf{k} & -\epsilon_\mathbf{k} \\ \Delta^*_{12}(\mathbf{k}) & 0 & -\epsilon^*_\mathbf{k} & -\xi_\mathbf{k} - g_\mathbf{k} \end{pmatrix}. \tag{12b}$$

The two bases are

$$\Psi^{(a)}_\mathbf{k} = (c_{\mathbf{k}1\uparrow} \quad c_{\mathbf{k}2\uparrow} \quad c^\dagger_{-\mathbf{k}1\downarrow} \quad c^\dagger_{-\mathbf{k}2\downarrow}), \tag{13a}$$

$$\Psi^{(b)}_\mathbf{k} = (c_{\mathbf{k}1\downarrow} \quad c_{\mathbf{k}2\downarrow} \quad c^\dagger_{-\mathbf{k}1\uparrow} \quad c^\dagger_{-\mathbf{k}2\uparrow}). \tag{13b}$$

In the above equations, $g_\mathbf{k} \equiv \hat{z}\cdot\mathbf{g}(\mathbf{k})$, $\Delta_{12}(\mathbf{k}) \equiv f_\mathbf{k} + i\, d_\mathbf{k}$, and $\Delta_{21}(\mathbf{k}) \equiv f_\mathbf{k} - i\, d_\mathbf{k}$, where 1,2 are sublattice labels. The two blocks are connected to each other by spin inversion $\uparrow\leftrightarrow\downarrow$, which leaves all matrix elements of $\hat{\mathcal{H}}^{(a)}(\mathbf{k})$ and $\hat{\mathcal{H}}^{(b)}(\mathbf{k})$ unchanged except for a change in the sign of the SOC term $g_\mathbf{k}$. However, as will be shown later, the Hall conductivity $\sigma_H(\omega)$ is an even function of $g_\mathbf{k}$. Therefore, we only need to focus on one block, say $\hat{\mathcal{H}}^{(a)}(\mathbf{k})$, and multiply the σ_H computed for that block by a factor of 2. An additional factor of $\frac{1}{2}$, arising from the double counting of degrees of freedom in BdG theory, will cancel this factor of 2. Hereafter, we drop the superscript (a) in $\hat{\mathcal{H}}^{(a)}(\mathbf{k})$ and simply denote it as $\hat{\mathcal{H}}(\mathbf{k})$ for brevity. Note that this decomposition into two 4×4 blocks is only possible in the absence of the intralayer p-wave pairing.

From $\hat{\mathcal{H}}(\mathbf{k})$ one can obtain the Bogoliubov quasiparticle energies, which have line nodes on the $k_z = \pm\pi$ plane that form six rings, as shown in Fig. 3. These nodal rings are counterexamples to Blount's theorem [42–47] and are topologically protected as a joint consequence of both the nonsymmorphic group symmetries and the nonzero spin-orbital coupling, as discussed in Refs. [45–47].

III. COMPUTATION OF THE ANOMALOUS HALL CONDUCTIVITY $\sigma_H(\omega)$

The Hall conductivity $\sigma_H(\omega)$ can be computed from the Kubo formula [19,48]

$$\sigma_H(\omega) = \frac{i}{2\omega}\lim_{\mathbf{q}\to 0}\{\pi_{xy}(\mathbf{q},\omega) - \pi_{yx}(\mathbf{q},\omega)\}, \tag{14}$$

where $\pi_{xy}(\mathbf{q},\omega)$ is the electric current density $\hat{J}_x$-$\hat{J}_y$ correlator. At the one-loop level π_{xy} is given by (setting $e = \hbar = c = 1$)

$$\begin{aligned}\pi_{xy}(\mathbf{q}=0,i\nu_m) = \sum_\mathbf{k} T\sum_n {\rm Tr}\{\hat{v}^x(\mathbf{k})\hat{G}(\mathbf{k},i\omega_n + i\nu_m)\\ \times\, \hat{v}^y(\mathbf{k})\hat{G}(\mathbf{k},i\omega_n)\},\end{aligned} \tag{15}$$

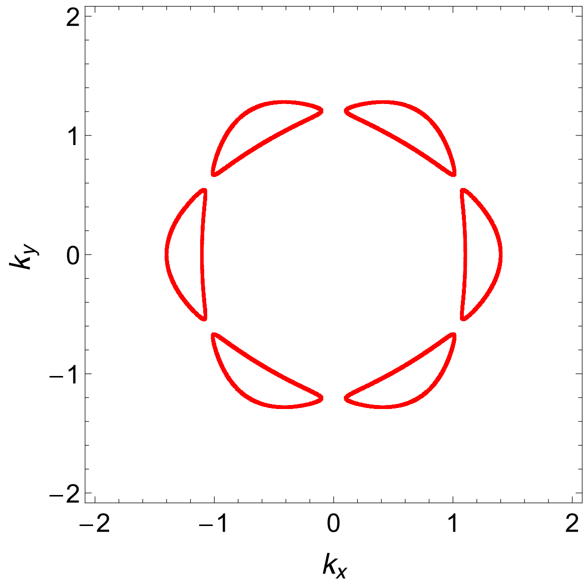

FIG. 3. Bogoliubov quasiparticle energy line nodes of the BdG Hamiltonian $\hat{\mathcal{H}}(\mathbf{k})$ at $k_z = \pi$. The parameter $\Delta_0 = 0.1\,t$. Other parameters used are the same as in Fig. 2.

where T is the temperature (set to $T = 0$ at the end of the calculation) and $\omega_n = (2n+1)\pi T$ and $\nu_m = 2m\pi T$ are fermionic and bosonic Matsubara frequencies, respectively. $\hat{G}(\mathbf{k},i\omega_n)$ is the Green's function of the 4×4 block Hamiltonian $\hat{\mathcal{H}}(\mathbf{k})$ with inverse defined by

$$\hat{G}^{-1}(\mathbf{k},i\omega_n) = i\omega_n - \hat{\mathcal{H}}(\mathbf{k}). \tag{16}$$

From $\det \hat{G}^{-1}(\mathbf{k},i\omega_n) = 0$ one obtains the Bogoliubov quasiparticle energies of the Hamiltonian $\hat{\mathcal{H}}(\mathbf{k})$. However, the equation to be solved is not a quadratic equation for ω_n^2 but a quartic equation in ω_n [see Eq. (A2) in Appendix A]. Consequently, the analytic expressions for the quasiparticle energies as well as the final expression for $\sigma_H(\omega)$ are quite lengthy, and these results are summarized in Appendix A in Eqs. (A4)–(A8b). From these expressions it is difficult to identify which ingredients are essential to obtain a nonzero $\sigma_H(\omega)$, and so we also compute σ_H perturbatively to obtain a much simpler expression that is valid at intermediate to high frequencies.

We treat the d-wave component of the superconducting order parameter as a perturbation and write $\hat{\mathcal{H}}(\mathbf{k}) = \hat{\mathcal{H}}_0(\mathbf{k}) + \hat{\mathcal{H}}'(\mathbf{k})$ where

$$\hat{\mathcal{H}}_0 = \begin{pmatrix} \xi_{\mathbf{k}} + g_{\mathbf{k}} & \epsilon_{\mathbf{k}} & 0 & f_{\mathbf{k}} \\ \epsilon_{\mathbf{k}}^* & \xi_{\mathbf{k}} - g_{\mathbf{k}} & f_{\mathbf{k}} & 0 \\ 0 & f_{\mathbf{k}}^* & -\xi_{\mathbf{k}} - g_{\mathbf{k}} & -\epsilon_{\mathbf{k}} \\ f_{\mathbf{k}}^* & 0 & -\epsilon_{\mathbf{k}}^* & -\xi_{\mathbf{k}} + g_{\mathbf{k}} \end{pmatrix} \tag{17}$$

and

$$\hat{\mathcal{H}}' = \begin{pmatrix} 0 & 0 & 0 & id_{\mathbf{k}} \\ 0 & 0 & -id_{\mathbf{k}} & 0 \\ 0 & id_{\mathbf{k}}^* & 0 & \\ -id_{\mathbf{k}}^* & 0 & 0 & 0 \end{pmatrix}. \tag{18}$$

$\hat{\mathcal{H}}_0$ and $\hat{\mathcal{H}}'$ will be taken as the "unperturbed" and "perturbed" Hamiltonian, respectively. We choose this particular partition because it is precisely the d-component superconducting order-parameter part that makes the Bogoliubov quasiparticle energy expression complicated [see Eq. (A2) in Appendix A] and also because, as we will see later, the leading-order contribution to σ_H is linear in $d_{\mathbf{k}}$.

Since we are including the effect of $\hat{\mathcal{H}}'$ only perturbatively, the results are only reliable for sufficiently large ω. Actually, the perturbative expansion is in $\beta_{\mathbf{k}} \propto i(f_{\mathbf{k}}d_{\mathbf{k}}^* - f_{\mathbf{k}}^*d_{\mathbf{k}})g_{\mathbf{k}}$, not just $d_{\mathbf{k}}$ [see Eq. (A2) in Appendix A for details]. So, the perturbative results are reliable for $\omega \gg \beta_{\mathbf{k}} \sim (\Delta_0^2\,\alpha)^{1/3}$, where α is the SOC strength. The full Green's function results and the perturbative results for $\sigma_H(\omega)$ are compared in Appendix A in Figs. 7 and 8, showing the two are essential identical beyond $\omega \gtrsim 4t$. Since the laser frequency at which the Kerr effect has been measured is $\omega \approx 0.8$ eV [5], which is $> 20t$ in our model, the perturbative results can be used to compare to experiment.

A. Perturbative calculation

Here, we discuss the perturbative calculation of σ_H, with further details given in Appendix B. Quantities of different order in $\hat{\mathcal{H}}'$ are represented by superscripts (0),(1),. . . . First, consider zeroth-order described by the Hamiltonian $\hat{\mathcal{H}}_0(\mathbf{k})$. The Bogoliubov quasiparticle energies $E_\pm$ are

$$E_\pm = \sqrt{a \pm \sqrt{a^2 - b}}, \tag{19}$$

with

$$a = \xi_{\mathbf{k}}^2 + g_{\mathbf{k}}^2 + |\epsilon_{\mathbf{k}}|^2 + |f_{\mathbf{k}}|^2, \tag{20a}$$

$$b = \left(\xi_{\mathbf{k}}^2 - g_{\mathbf{k}}^2 + |f_{\mathbf{k}}|^2 - |\epsilon_{\mathbf{k}}|^2\right)^2 + |f_{\mathbf{k}}|^2(\epsilon_{\mathbf{k}} + \epsilon_{\mathbf{k}}^*)^2, \tag{20b}$$

which are slightly different from those of the full Hamiltonian $\hat{\mathcal{H}}(\mathbf{k})$. However, E_- still has nodal rings on the $k_z = \pm\pi$ plane that are almost identical to those obtained from the full Hamiltonian $\hat{\mathcal{H}}(\mathbf{k})$, plotted in Fig. 3. These nodal rings are protected by the nonsymmorphic space-group symmetry and spin-orbit coupling [35,45].

The velocity operators, which appear in Eq. (15), are defined by the normal-state Hamiltonian $\hat{\mathcal{H}}_N(\mathbf{k})$, which can be written in terms of the sublattice Pauli matrices σ_α:

$$\hat{\mathcal{H}}_N(\mathbf{k}) = \xi_{\mathbf{k}}\sigma_0 + \mathbf{h}\cdot\boldsymbol{\sigma}, \tag{21}$$

with $\mathbf{h} = (\frac{\epsilon_{\mathbf{k}}}{\sqrt{2}}, \frac{\epsilon_{\mathbf{k}}^*}{\sqrt{2}}, g_{\mathbf{k}})$ and $\boldsymbol{\sigma} = (\sigma_+,\sigma_-,\sigma_3)$. Then, $\hat{v}^x = \partial_{k_x}\hat{\mathcal{H}}_N(\mathbf{k})\,\tau_0$ [15,19], where τ_0 is the identity matrix for the Nambu space or, written out explicitly,

$$\hat{v}^x = \begin{pmatrix} \partial_{k_x}E_a(\mathbf{k}) & \partial_{k_x}\epsilon_{\mathbf{k}} & 0 & 0 \\ \partial_{k_x}\epsilon_{\mathbf{k}}^* & \partial_{k_x}E_b(\mathbf{k}) & 0 & 0 \\ 0 & 0 & \partial_{k_x}E_a(\mathbf{k}) & \partial_{k_x}\epsilon_{\mathbf{k}} \\ 0 & 0 & \partial_{k_x}\epsilon_{\mathbf{k}}^* & \partial_{k_x}E_b(\mathbf{k}) \end{pmatrix}, \tag{22}$$

with $E_a(\mathbf{k}) \equiv \xi_{\mathbf{k}} + g_{\mathbf{k}}$ and $E_b(\mathbf{k}) \equiv \xi_{\mathbf{k}} - g_{\mathbf{k}}$. $\hat{v}^y$ can be obtained from $\hat{v}^x$ by the substitution $\partial_{k_x} \to \partial_{k_y}$. With $\hat{v}^x,\hat{v}^y$ and $\hat{G}^{(0)} \equiv \{i\omega_n - \hat{\mathcal{H}}_0(\mathbf{k})\}^{-1}$, one can compute the zeroth-order current-current correlator $\pi_{xy}^{(0)}(i\nu_m)$ from Eq. (15). However, a direct computation shows that $\pi_{xy}^{(0)}(i\nu_m) - \pi_{yx}^{(0)}(i\nu_m) = 0$, so that $\sigma_H^{(0)}(\omega) \equiv 0$. In other words, a chiral f-wave superconducting order parameter alone does not give rise to a nonzero anomalous Hall conductivity from the multiband mechanism if the two bands arise from ABAB stacking. The mixing between f- and d-wave components is crucial for a nonzero σ_H and one needs to go to first order to calculate a nonzero $\sigma_H(\omega)$.

From the full Green's function $\hat{G} = \hat{G}^{(0)} + \hat{G}^{(0)}\hat{\mathcal{H}}'\hat{G}^{(0)} + \dots$, one can define the first-order Green's function as $\hat{G}^{(1)} = \hat{G}^{(0)}\hat{\mathcal{H}}'\hat{G}^{(0)}$ and, from Eq. (15), the first-order current-current correlator is

$$\pi_{xy}^{(1)}(i\nu_m) = \sum_{\mathbf{k}} T \sum_n \{\mathrm{Tr}[\hat{v}^x \hat{G}^{(0)}(\mathbf{k},i\omega_n + i\nu_m)\hat{v}^y \times \hat{G}^{(1)}(\mathbf{k},i\omega_n)] + \{(0) \leftrightarrow (1)\}\}. \tag{23}$$

This [or, more precisely, $\pi_{xy}^{(1)}(i\nu_m) - \pi_{yx}^{(1)}(i\nu_m)$] is evaluated in Appendix B by first writing the velocity operators and Green's functions as linear combinations of Pauli matrices to simplify computing the trace and then doing the Matsubara sum. After performing a Wick rotation $i\nu_m \to \omega + i\delta$, one obtains the final expression for the Hall conductivity

$$\sigma_H^{(1)}(\omega) = \sum_{\mathbf{k}} 4i[f_{\mathbf{k}}d_{\mathbf{k}}^* - f_{\mathbf{k}}^* d_{\mathbf{k}}]\,\xi_{\mathbf{k}}\left\{8i\ g_k\ \mathbf{h}\cdot\partial_{k_x}\mathbf{h}\times\partial_{k_y}\mathbf{h} \times \frac{S_{\mathbf{k}}(\omega)}{\omega} + \Omega_{xy}\frac{T_{\mathbf{k}}(\omega)}{\omega}\right\}, \tag{24}$$

where for brevity we have suppressed the infinitesimal imaginary part $i\delta$ in $\omega + i\delta$. Ω_{xy} is an antisymmetrized velocity factor given by

$$\Omega_{xy} \equiv -i\left[\partial_{k_x}\epsilon_{\mathbf{k}}\partial_{k_y}\epsilon_{\mathbf{k}}^* - \partial_{k_x}\epsilon_{\mathbf{k}}^*\partial_{k_y}\epsilon_{\mathbf{k}}\right]. \tag{25}$$

We have also introduced two frequency-dependent functions in Eq. (24), which are defined as (for details see Appendix B)

$$\frac{S_{\mathbf{k}}(\omega)}{\omega} \equiv F_1(\mathbf{k},\omega) - \frac{\xi_{\mathbf{k}}^2 - g_{\mathbf{k}}^2 - |\epsilon_{\mathbf{k}}|^2}{E_+E_-}F_2(\mathbf{k},\omega) \tag{26}$$

and

$$\frac{T_{\mathbf{k}}(\omega)}{\omega} \equiv F_3(\mathbf{k},\omega), \tag{27}$$

with $F_1(\mathbf{k},\omega)$, $F_2(\mathbf{k},\omega)$, and $F_3(\mathbf{k},\omega)$ given by

$$F_1(\mathbf{k},\omega) \approx \frac{C_{++}}{\omega^2 - 4E_+^2} + \frac{C_{--}}{\omega^2 - 4E_-^2} + \frac{C_{+-}}{\omega^2 - (E_+ + E_-)^2}, \tag{28a}$$

$$F_2(\mathbf{k},\omega) \approx \frac{D_{++}}{\omega^2 - 4E_+^2} + \frac{D_{--}}{\omega^2 - 4E_-^2} + \frac{D_{+-}}{\omega^2 - (E_+ + E_-)^2}, \tag{28b}$$

$$F_3(\mathbf{k},\omega) \approx \frac{B_{+-}}{\omega^2 - (E_+ + E_-)^2}. \tag{28c}$$

The $\approx$ sign means only the leading-order terms in $f_{\mathbf{k}}$ and $d_{\mathbf{k}}$ have been kept. There are seven frequency-independent coefficients in the numerators of F_1, F_2, and F_3. Their expressions are

$$C_{++} = -D_{--} = \frac{E_+}{(E_-^2 - E_+^2)^3}, \tag{29a}$$

$$D_{++} = -C_{--} = \frac{E_-}{(E_-^2 - E_+^2)^3}, \tag{29b}$$

$$C_{+-} = \frac{E_+^2 + E_-^2}{2E_+E_-(E_+ + E_-)^3(E_+ - E_-)^2}, \tag{29c}$$

$$D_{+-} = \frac{-1}{(E_+ + E_-)^3(E_+ - E_-)^2}, \tag{29d}$$

$$B_{+-} = \frac{1}{2E_+E_-(E_+ + E_-)}. \tag{29e}$$

The subscripts $\{++, --, +-\}$ in these coefficients directly reflect the corresponding physical processes that they are associated with, which can be inferred from the denominator of each term in the expressions of $F_1(\mathbf{k},\omega)$, $F_2(\mathbf{k},\omega)$, and $F_3(\mathbf{k},\omega)$. For example, the first term in $F_1(\mathbf{k},\omega)$ with coefficient C_{++} corresponds to a process where a Cooper pair, with momentum $(\mathbf{k},-\mathbf{k})$, is broken and a Bogoliubov quasiparticle pair with energies $E_+(\mathbf{k})$ and $E_+(-\mathbf{k})$ are excited by the incident photon with a frequency ω. The two Bogoliubov quasiparticles have the same momentum $(\mathbf{k},-\mathbf{k})$ as the broken Cooper pair because the incident photon momentum $\mathbf{q} \approx 0$ relative to $\mathbf{k}$. Energy conservation of this process requires $\omega = E_+(\mathbf{k}) + E_+(-\mathbf{k}) = 2E_+$, which explains the denominator $\omega^2 - (2E_+)^2$ in the first term in $F_1(\mathbf{k},\omega)$. Other terms in $F_1(\mathbf{k},\omega)$, $F_2(\mathbf{k},\omega)$, and $F_3(\mathbf{k},\omega)$ can be interpreted in a similar way. Notice that in the expressions for $F_1(\mathbf{k},\omega)$, $F_2(\mathbf{k},\omega)$, and $F_3(\mathbf{k},\omega)$ there is no term with a denominator $\omega^2 - (E_+ - E_-)^2$, which would correspond to a $T > 0$ process where a preexisting Bogoliubov quasiparticle with an energy E_- gets excited to a higher-energy level of E_+ by the incident photon.

Finally, as noted below Eq. (13b), we can see from Eqs. (26) and (27) that $\sigma_H^{(1)}(\omega)$ is an even function of $g_{\mathbf{k}}$ since the two functions $S_{\mathbf{k}}(\omega)$ and $T_{\mathbf{k}}(\omega)$ depend on $\mathbf{k}$ only through $E_\pm$, which are even in $g_{\mathbf{k}}$ [see Eq. (19)]; Ω_{xy} does not depend on $g_{\mathbf{k}}$ [see Eq. (25)], and the factor $g_k\ \mathbf{h}\cdot\partial_{k_x}\mathbf{h}\times\partial_{k_y}\mathbf{h}$ is also even in $g_{\mathbf{k}}$ because the mixed product contributes one and only one $g_{\mathbf{k}}$ since $\mathbf{h} = (\epsilon_{\mathbf{k}}/\sqrt{2},\epsilon_{\mathbf{k}}^*/\sqrt{2},g_{\mathbf{k}})$.

Next, we evaluate the expression for $\sigma_H^{(1)}(\omega)$ in Eq. (24) numerically. Replacing ω with $\omega + i\delta$ in Eq. (24), the imaginary part can be written as

$$\mathrm{Im}\,\sigma_H^{(1)} = -\frac{\pi}{2\omega}\sum_{\mathbf{k}} 4i\,[f_{\mathbf{k}}d_{\mathbf{k}}^* - f_{\mathbf{k}}^*d_{\mathbf{k}}]\,\xi_{\mathbf{k}}\big\{8i\ g_{\mathbf{k}}\mathbf{h}\cdot\partial_{k_x}\mathbf{h} \times \partial_{k_y}\mathbf{h}\,\mathcal{A}_1(\mathbf{k},\omega) + \Omega_{xy}\,\mathcal{A}_2(\mathbf{k},\omega)\big\}, \tag{30}$$

where $\mathcal{A}_1(\mathbf{k},\omega)$ and $\mathcal{A}_2(\mathbf{k},\omega)$ are

$$\mathcal{A}_1(\mathbf{k},\omega) \equiv \left[C_{++} - \frac{\xi_{\mathbf{k}}^2 - g_{\mathbf{k}}^2 - |\epsilon_{\mathbf{k}}|^2}{E_+E_-}D_{++}\right] \times \{\delta(\omega - 2E_+) + \delta(\omega + 2E_+)\} + \left[C_{--} - \frac{\xi_{\mathbf{k}}^2 - g_{\mathbf{k}}^2 - |\epsilon_{\mathbf{k}}|^2}{E_+E_-}D_{--}\right] \times \{\delta(\omega - 2E_-) + \delta(\omega + 2E_-)\}$$

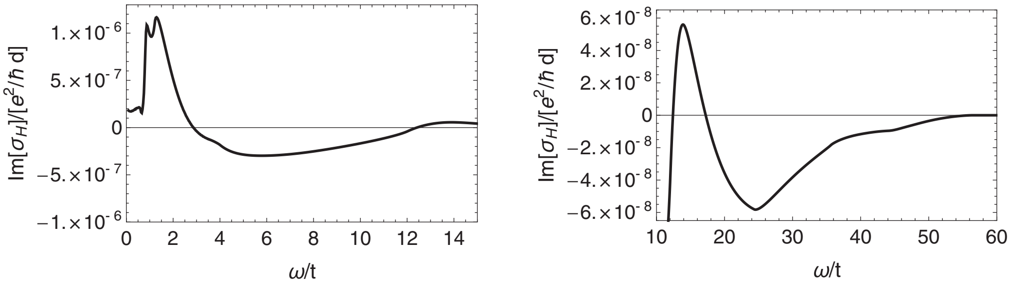

FIG. 4. Numerical results for Im $\sigma_H^{(1)}(\omega)$. Left panel: small frequency regime $\omega/t \leqslant 14$; right panel: large frequency regime $\omega/t \geqslant 10$. Note that the vertical axis scales of the two figures are different. The unit of σ_H is $e^2/\hbar d$, with d the $\hat{c}$-axis lattice spacing of UPt$_3$. Parameters used are $(t,t_z,t',\alpha,\mu,\Delta_0,\eta) = (1,-4,1,2,12,0.1,1.0)$.

$$+\left[C_{+-} - \frac{\xi_{\mathbf{k}}^2 - g_{\mathbf{k}}^2 - |\epsilon_{\mathbf{k}}|^2}{E_+E_-} D_{+-}\right]$$
$$\times \{\delta[\omega - (E_+ + E_-)] + \delta[\omega + (E_+ + E_-)]\}, \tag{31a}$$

$$\mathcal{A}_2(\mathbf{k},\omega) \equiv B_{+-}\ \{\delta[\omega - (E_+ + E_-)] + \delta[\omega + (E_+ + E_-)]\}. \tag{31b}$$

The $\mathbf{k}$ summation in Eq. (30) is calculated numerically for each ω and the results are plotted in Fig. 4 over two different ranges of ω/t so that the details at larger ω/t, where $|\mathrm{Im}\,\sigma_H^{(1)}|$ is smaller, can be clearly seen. $\mathrm{Im}\,\sigma_H^{(1)}(\omega)$ has several sign changes as a function of ω because the different factors in Eq. (30) change sign at different $\mathbf{k}$ positions with different quasiparticle energies. Also, note that $\mathrm{Im}\,\sigma_H^{(1)}(\omega)$ is nonzero for arbitrarily small ω since the external field can excite quasiparticle pairs at arbitrarily small energy near the line nodes in the superconducting gap. Although $\sigma_H^{(1)}(\omega)$ vanishes as $\omega \to 0$, this feature is not visible in Fig. 4 (left panel) because the crossover to small-ω behavior occurs at very small frequency $\omega < 0.01t$ (see Fig. 6 of Ref. [35]).

The real part $\mathrm{Re}\,\sigma_H^{(1)}(\omega)$ can be computed from the data for $\mathrm{Im}\,\sigma_H^{(1)}(\omega)$ by the Kramers-Kronig transformation

$$\mathrm{Re}\,\sigma_H^{(1)}(\omega) = \frac{2}{\pi}\mathcal{P}\int_0^\infty \frac{\nu\ \mathrm{Im}\ \sigma_H^{(1)}(\nu)}{\nu^2 - \omega^2} d\nu, \tag{32}$$

where $\mathcal{P}$ stands for Cauchy principal value integral. The results for $\mathrm{Re}\,\sigma_H^{(1)}(\omega)$ are plotted in Fig. 5. In the right panel of Fig. 5, the red dashed line is an exact high-frequency asymptotic result, whose expression is given by [49]

$$\sigma_H(\omega \to \infty) = \frac{i}{\omega^2}\langle[\hat{J}_x,\hat{J}_y]\rangle + O\left(\frac{1}{\omega^4}\right), \tag{33}$$

where $[\hat{J}_x,\hat{J}_y]$ is an equal-time commutator and the expectation value $\langle\dots\rangle$ is with respect to the ground state of the BdG Hamiltonian. In Appendix C, we compute $\langle[\hat{J}_x,\hat{J}_y]\rangle$ to first order in $\hat{\mathcal{H}}'$ and find $\langle[\hat{J}_x,\hat{J}_y]\rangle^{(1)} \approx -i\,2.2\times10^{-5}t^2\,e^2/(\hbar\,d)$. Similar to $\mathrm{Im}\,\sigma_H^{(1)}(\omega)$, $\mathrm{Re}\,\sigma_H^{(1)}(\omega)$ has further structure at very low frequency, $\omega < 0.01t$. It saturates to a constant with a zero slope as $\omega \to 0$. Again, due to the large frequency range in Fig. 5 (left panel), this feature is not visible.

B. Discussions of $\sigma_H^{(1)}$

From Eq. (24), we can identify the necessary ingredients for $\sigma_H^{(1)}$ to be nonzero. As emphasized previously, both the chiral f-wave and the chiral d-wave components need to be present. In particular, the dependence of $\sigma_H^{(1)}$ on these two parameters is through the combination $i[f_{\mathbf{k}}d_{\mathbf{k}}^* - f_{\mathbf{k}}^*d_{\mathbf{k}}]$, which is proportional to the chirality. Under time reversal, this combination, and consequently $\sigma_H^{(1)}$, changes sign. This can be seen explicitly from the fact that under time reversal, $\Delta_{12}(\mathbf{k}) \to -\Delta_{12}^*(-\mathbf{k})$, $\Delta_{21}(\mathbf{k}) \to -\Delta_{21}^*(-\mathbf{k})$, and $2i[f_{\mathbf{k}}d_{\mathbf{k}}^* - f_{\mathbf{k}}^*d_{\mathbf{k}}] = \Delta_{21}(\mathbf{k})\Delta_{21}^*(\mathbf{k}) - \Delta_{12}(\mathbf{k})\Delta_{12}^*(\mathbf{k})$. This is the only combination quadratic in Δ_{12} and/or Δ_{21} that is odd under time reversal. It is also this term that makes the order parameter $\hat{\Delta}(\mathbf{k})$ nonunitary.

The second important ingredient for σ_H is the complex intersublattice hopping $\epsilon_{\mathbf{k}}$ since both velocity terms appearing in Eq. (24), $\mathbf{h}\cdot\partial_{k_x}\mathbf{h}\times\partial_{k_y}\mathbf{h}$ and Ω_{xy}, vanish if $\epsilon_{\mathbf{k}}$ is real. These

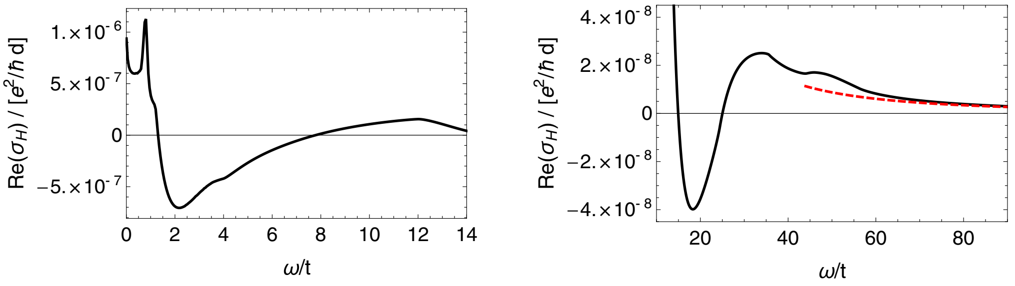

FIG. 5. Numerical results for Re $\sigma_H^{(1)}(\omega)$. Left panel: small frequency regime; right panel: large frequency regime. Note that the scales of the vertical axes in the two figures are different. In the right figure, the red dashed line is a high-frequency asymptotic result. Parameters used are the same as in Fig. 4.

velocity terms are consistent with another general requirement for σ_H to be nonzero in the multiband mechanism. Namely, some antisymmetrized products of the velocity operators $v^x_{ab}v^y_{cd} - v^y_{ab}v^x_{cd}$ (where a,b label orbitals or, in our case, sublattices) need to be nonzero. Note that SOC, $g_{\mathbf{k}}$, is not necessary for a nonzero σ_H. Of the two terms in Eq. (24), only the first term vanishes if $g_{\mathbf{k}} = 0$. The second term, with Ω_{xy}, only depends on $g_{\mathbf{k}}$ through the Bogoliubov quasiparticle energies $E_\pm$ and remains nonzero if the SOC is absent.

The two key ingredients identified above, the mixing of the chiral f- and d-wave order parameters and the complex intersublattice hopping $\epsilon_{\mathbf{k}}$, are both direct consequences of the nonsymmorphic symmetry of UPt$_3$. They would both be absent if the lattice were symmorphic. In this sense, the terms that we have identified for σ_H are unique to nonsymmorphic chiral superconductors.

The two terms in Eq. (24) can be represented by Feynman diagrams, which are shown in Fig. 6. For each diagram in Fig. 6, the time-reversed diagram needs to be subtracted.

There are two types of diagrams. In Fig. 6(a), only one of the two vertices involves two different orbitals, while in Fig. 6(b) both the vertices involve transitions between different orbitals. Of the two terms in Eq. (24), the term $\propto\Omega_{xy}$ only contributes to Fig. 6(b), while the other term, $\propto\mathbf{h}\cdot\partial_{k_x}\mathbf{h}\times\partial_{k_y}\mathbf{h}$, is a mixture of Figs. 6(a) and 6(b). This is because $\mathbf{h}\cdot\partial_{k_x}\mathbf{h}\times\partial_{k_y}\mathbf{h}$ can be written as a sum of $\epsilon_{\mathbf{k}}\partial_{k_x}\epsilon^*_{\mathbf{k}}\partial_{k_y}g_{\mathbf{k}} + \epsilon^*_{\mathbf{k}}\partial_{k_x}g_{\mathbf{k}}\partial_{k_y}\epsilon_{\mathbf{k}} - \{x \leftrightarrow y\}$ and $g_{\mathbf{k}}\partial_{k_x}\epsilon_{\mathbf{k}}\partial_{k_y}\epsilon^*_{\mathbf{k}} - \{x \leftrightarrow y\}$, of which the former and latter correspond to Figs. 6(a) and 6(b), respectively. In the band basis, the Ω_{xy} term in Eq. (24) corresponds to Fig. 6(a) (with i,j now labeling bands), rather than Fig. 6(b) as in the orbital basis, while the whole $\mathbf{h}\cdot\partial_{k_x}\mathbf{h}\times\partial_{k_y}\mathbf{h}$ term corresponds to Fig. 6(b). It is clear in the band basis that both Figs. 6(a) and 6(b) vanish if the interband pairing is zero, similar to what was found in Ref. [19].

Note that Fig. 6(b) type of diagram is absent in Ref. [19] because the model studied there has a real interorbital hopping $\epsilon_{\mathbf{k}}$, which makes the contribution from Fig. 6(b) with the photon polarization $(i,j) = (x,y)$ exactly cancel the same diagram with $(i,j) = (y,x)$. On the other hand, Fig. 6(a) vanishes in the current model unless $\epsilon_{\mathbf{k}}$ is complex, while it survives in Ref. [19] for real interorbital hopping, due to the different way the interorbital pairing arises in the two models.

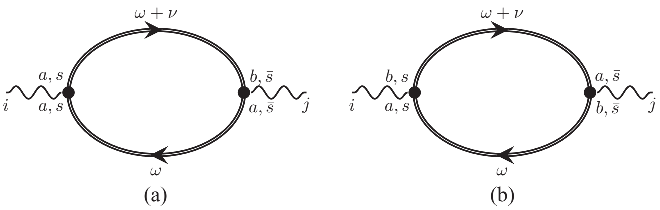

FIG. 6. Diagrammatic representation of the nonvanishing contributions to σ_H, where wiggly lines are photons and double solid lines with arrows are Green's functions given by Eq. (16). The photon polarization is labeled by $i,j = x,y$. a,b are sublattice labels, and s is the spin label. If $s = \{\uparrow,\downarrow\}$, then $\bar{s} = \{\downarrow,\uparrow\}$. Note that, in each diagram, the spin labels on a right vertex are opposite to that on the corresponding left vertex. This is because, in each diagram, each Green's function contributes one superconducting order parameter that pairs electrons of opposite spin, while all normal-state Hamiltonian matrix elements, including SOC, only connect electrons of the same spin.

$\sigma_H(\omega)$ also needs to obey the following two sum rules [50,51]:

$$\int_0^\infty d\omega\,\mathrm{Re}\,\sigma_H(\omega) = 0, \tag{34}$$

$$\int_{-\infty}^{\infty} d\omega\,\frac{\omega\,\mathrm{Im}\,\sigma_H(\omega)}{\pi} = -i\langle[\hat{J}_x,\hat{J}_y]\rangle, \tag{35}$$

where Eq. (35) is analogous to the well-known optical conductivity f-sum rule. In Appendix C, we show these sum rules are satisfied, both analytically and numerically, by $\sigma^{(1)}_H(\omega)$.

Lastly, we mention that the Hall conductivity, quite generally, needs to satisfy several symmetry constraints. Under time reversal, all vertical mirror reflections, and particle-hole interchange, σ_H must reverse its sign. Both $\sigma^{(1)}_H$ given in Eq. (24), and the full Green's function result of σ_H given in Appendix A are consistent with these symmetry constraints.

IV. ESTIMATION OF THE KERR ROTATION ANGLE θ_K

From the numerical results of $\sigma_H(\omega)$, the Kerr rotation angle θ_K can be estimated using Eq. (1), which also involves the complex index of refraction $n(\omega)$. Here, we use our results to estimate the Kerr angle for UPt$_3$, where θ_K was measured [5] at a laser frequency $\omega \approx 0.8$ eV.

We first estimate $n(\omega = 0.8\text{ eV})$ from experimental data. By definition $n(\omega) = \sqrt{\epsilon(\omega)}$, where $\epsilon(\omega)$ is related to the conductivity $\sigma(\omega)$ by $\epsilon(\omega) = \epsilon_\infty + i4\pi\sigma(\omega)/\omega$ and ϵ_∞ is the high-frequency limit dielectric constant. We extract $\sigma(\omega = 0.8\text{ eV}) \approx (1.7 + i\,0.4)\times 10^{15}\text{ s}^{-1}$ from the experimental data of Ref. [52]. Taking $\epsilon_\infty = 1$, we obtain $\epsilon(\omega = 0.8\text{ eV}) \approx -3.1 + i\,17.5$, which gives an index of refraction

$$n(\omega = 0.8\text{ eV}) \approx 2.7 + i\,3.2. \tag{36}$$

To obtain a value for $\sigma_H(\omega \approx 0.8\text{ eV})$, we need to estimate the in-plane hopping parameter t in eV since we have scaled all energies by t. This can be obtained by comparing the normal-state band dispersions of our two-band model along the symmetry directions A − L − H − A in the $k_z = \pi$ plane to the corresponding first-principles calculation results from Ref. [53]. The comparison gives $t \approx 36$ meV (for details, see Appendix D). This value of t corresponds to $\omega/t \approx 22.2$ at $\omega = 0.8$ eV. From our numerical results for $\sigma_H(\omega)$ in Figs. 4 and 5 we obtain, at $\omega/t \approx 22.2$,

$$\sigma_H(\omega \approx 0.8\text{ eV}) \approx -(2.3 + i\,5.1)\times 10^{-8}\frac{e^2}{\hbar d}, \tag{37}$$

where $d = 4.9$ Å is the c-axis lattice spacing of UPt$_3$. From Eqs. (36), (37), and (1), the Kerr angle is then

$$\theta_K \approx 34\times 10^{-9}\text{ rad}. \tag{38}$$

Our estimated θ_K is about an order of magnitude smaller than the experimental value of about 350 nanoradians measured at the lowest temperatures [5]. However, it may still be a significant contribution to the explanation for the Kerr measurement on $\mathrm{UPt_3}$ [5] given that there are uncertainties in the optical constants, the band parameters, and the magnitude of Δ_0 used for this estimate. We briefly comment on these uncertainties.

Ideally, one would like measurements of $n(\omega)$ on the same crystal used for the Kerr measurements. Other optical data on $\mathrm{UPt_3}$ would give somewhat different results [54–56], although we estimate that the uncertainty in the optical data is unlikely to change the estimated Kerr angle by more than a factor of 3 or so.

As to the band parameters, uncertainty comes both from the value of t and from the fact that a very simplified nearest-neighbor hopping model has been used to approximate the two bands which give rise to the starfish Fermi surface. This likely introduces a larger uncertainty than that from errors in the estimate of $n(\omega)$.

The other parameter that can greatly affect the size of θ_K is Δ_0, the amplitude of the gap function written in the orbital basis. Note that Δ_0 is not the gap that one would observe in tunneling measurements. Defining Δ_g as the position of the coherence peak in the Bogoliubov quasiparticle density of states spectrum, one finds $\Delta_g \approx 0.16\,\Delta_0$ (see Fig. 6 of Ref. [35]). Experiments have found values for Δ_g of 0.04 meV [57], 0.1 meV [58], and more recently 0.5 meV [31]. The parameters we used, taken from Yanase [35], with $t = 36$ meV, correspond to $\Delta_g = 0.58$ meV, roughly consistent with the most recent experimental value. Since the Kerr angle scales quadratically with the gap magnitude, smaller values of Δ_g would give much smaller values of θ_K. For example, setting $T_c = 0.53$ K, we find $\Delta_g \approx 0.11$ meV for our model in the weak-coupling limit, which would reduce θ_K by a factor of 26.

Lastly, there are several other Fermi surface sheets that we did not take into account, which might contribute to θ_K. These additional contributions could either increase or decrease the total θ_K, depending on their relative magnitude and sign.

With these uncertainties in mind, we conclude that the θ_K that we have identified here can be significant for explaining the Kerr measurement on $\mathrm{UPt_3}$, even if it is not large enough to account for the whole experimentally observed signal. Further experiments and theoretical studies are needed to resolve the above uncertainties.

V. CONCLUSION AND DISCUSSIONS

To summarize, by considering a simplified two-band model that results from ABAB stacking for the starfishlike Fermi surface of $\mathrm{UPt_3}$, we have identified a contribution to the ac anomalous Hall conductivity for $\mathrm{UPt_3}$ within the intrinsic multiband chiral superconductivity mechanism. The Kerr angle estimated from the computed Hall conductivity can be significant for understanding the Kerr measurement on $\mathrm{UPt_3}$. This mechanism requires nonzero interband pairing. Since intraband and interband pairing are indistinguishable at the six points on the $k_z = \pm\pi$ plane where the starfishlike Fermi surfaces of $\mathrm{UPt_3}$ intersect, this is a useful model for studying the multiband chiral superconductivity mechanism.

We have identified two crucial ingredients for the nonzero σ_H: a complex intersublattice hopping between U sites and a superconducting order parameter that involves mixing between chiral f-wave and chiral d-wave pairing. Both of these are consequences of the nonsymmorphic group symmetry of the $\mathrm{UPt_3}$ crystal lattice. If the intersublattice hopping is real or if one of the chiral f- and d-wave pairing components is absent, then σ_H and θ_K vanish. This is a generalization of, albeit somewhat distinct from, the multiband chiral superconductivity mechanism for the anomalous ac Hall effect in a chiral p-wave superconductor [19]. The σ_H and θ_K contribution that we have discussed here can also be applied to other nonsymmorphic chiral superconductors.

In our analysis we have identified two types of terms that contribute to $\sigma_H(\omega)$ at each $\mathbf{k}$ point, as can be seen from Eq. (24). One term does not require SOC, while the other does. The two make comparable contributions to σ_H. However, these two contributions in general can have different signs at different $\mathbf{k}$ points, which results in multiple sign changes of $\sigma_H(\omega)$ as a function of ω. Because of these sign changes, the estimated Kerr angle can be sensitive to the band parameters as well as to the laser frequency used in the Kerr measurement. Therefore, future Kerr measurements at different frequencies would be very helpful in determining how relevant the Kerr angle contribution identified here is to $\mathrm{UPt_3}$.

We should mention that in our calculation we have neglected a small chiral p-wave component pairing in the original proposed superconducting order parameter of Ref. [35]. This component is also symmetry allowed but is expected to be energetically less favorable compared with the dominant chiral f and d components. In the two-band model, we consider, this p-wave component alone can also give rise to a nonzero $\sigma_H(\omega)$. This contribution relies on the nonunitary nature of the p-wave pairing (it pairs only one spin component if $\eta = 1$), and requires nonzero SOC and complex intersublattice hopping. Presumably, the admixture of this neglected small p-wave component will not significantly alter the estimated Kerr angle simply because its pairing amplitude is thought to be very small.

Recently, the authors of Ref. [59] suggested that the Kerr rotation in $\mathrm{UPt_3}$ can not be understood without invoking pairing in completely filled or empty bands because the laser frequency used in the Kerr angle measurement [5], $\omega \approx 0.8\,\mathrm{eV}$, is bigger than the normal-state bandwidth of the partially filled bands of $\mathrm{UPt_3}$. However, this does not need to be the case for two reasons. First, since the incident photon breaks a Cooper pair and generates two Bogoliubov quasiparticles, the maximum energy cost is not the bandwidth, but twice the energy difference between the Fermi level and the bottom or top of the band (whichever is greater). From Ref. [60], this maximum energy along the symmetry direction A – L – H – A in the $k_z = \pi$ plane is about 0.68 eV, while from Ref. [53], this is about 0.84 eV. The latter (which we used to determine the hopping t in our model) allows energy-conserving transitions within the band at 0.8 eV. Second, both $\mathrm{Re}\,\sigma_H(\omega)$ and $\mathrm{Im}\,\sigma_H(\omega)$ can make significant contributions to θ_K. Even if the laser frequency is larger than the excitation energy of two quasiparticles within the band, $\mathrm{Re}\,\sigma_H(\omega)$ will still be nonzero at $\omega = 0.8$ eV. Consequently, the observation of nonzero θ_K in UPt$_3$ at 0.8 eV may still be understood within a model of partially filled bands.

ACKNOWLEDGMENTS

We would like to thank T. Timusk and S. Kivelson for helpful discussions. This work is supported in part by NSERC (C.K. and Z.W.), the Canada Research Chair program (C.K.), the National Science Foundation under Grant No. NSF PHY11-25915 (A.J.B., C.K., G.Z.), the Gordon and Betty Moore Foundation's EPiQS Initiative through Grant No. GBMF4302 (A.J.B. and C.K.), the ANR-DFG grant Fermi-NESt (G.Z.), and a grant from the Simons Foundation (Grant No. 395604 to C.K.). A.J.B., C.K., and G.Z. greatly appreciate the hospitality provided by the Kavli Institute for Theoretical Physics at UCSB and (for A.J.B., C.K., and Z.W.) the hospitality of the Stanford Institute for Theoretical Physics, where part of the work was completed.

APPENDIX A: FULL GREEN'S FUNCTION CALCULATION OF $\sigma_H(\omega)$

As mentioned in the main text, the full Green's function calculation is much more involved than the perturbative calculation. Here, we present some main steps for the full calculation of $\sigma_H(\omega)$, omitting detail of derivations.

We first establish some notation. We denote the four Bogoliubov quasiparticle energies of the BdG Hamiltonian $\hat{\mathcal{H}}^{(a)}(\mathbf{k})$, from Eq. (12a) of the main text, as E_i, with $i = \{1,2,3,4\}$. The E_i are solutions to

$$\det\{\omega - \hat{\mathcal{H}}^{(a)}(\mathbf{k})\} = 0, \tag{A1}$$

which can be expanded as

$$\omega^4 + \alpha_{\mathbf{k}}\,\omega^2 + \beta_{\mathbf{k}}\,\omega + \gamma_{\mathbf{k}} = 0, \tag{A2}$$

where the three coefficients are given by

$$\alpha_{\mathbf{k}} = -2\big(\xi_{\mathbf{k}}^2 + g_{\mathbf{k}}^2 + |f_{\mathbf{k}}|^2 + |d_{\mathbf{k}}|^2 + |\epsilon_{\mathbf{k}}|^2\big), \tag{A3a}$$

$$\beta_{\mathbf{k}} = 4i\,(f_{\mathbf{k}}d_{\mathbf{k}}^* - f_{\mathbf{k}}^*d_{\mathbf{k}})\,g_{\mathbf{k}}, \tag{A3b}$$

$$\begin{aligned}\gamma_{\mathbf{k}} = {}&\big(\xi_{\mathbf{k}}^2 - g_{\mathbf{k}}^2 - |\epsilon_{\mathbf{k}}|^2 + |f_{\mathbf{k}}|^2 + |d_{\mathbf{k}}|^2\big)^2 + 4|d_{\mathbf{k}}|^2|\epsilon_{\mathbf{k}}|^2\\ &+ (|f_{\mathbf{k}}|^2 - |d_{\mathbf{k}}|^2)(\epsilon_{\mathbf{k}} + \epsilon_{\mathbf{k}}^*)^2 + (f_{\mathbf{k}}^*d_{\mathbf{k}} - f_{\mathbf{k}}d_{\mathbf{k}}^*)^2\\ &- i(f_{\mathbf{k}}d_{\mathbf{k}}^* + f_{\mathbf{k}}^*d_{\mathbf{k}})\big(\epsilon_{\mathbf{k}}^2 - (\epsilon_{\mathbf{k}}^*)^2\big).\end{aligned} \tag{A3c}$$

Equation (A2) is a quartic equation for ω rather than a quadratic equation in ω^2 due to the $\beta_{\mathbf{k}}\omega$ term. Because of this, the solutions E_i do not occur as $\{+E,-E\}$ particle-hole pairs. However, this does not contradict the particle-hole symmetry of the full superconducting BdG Hamiltonian which is restored when $\hat{\mathcal{H}}^{(a)}$ is combined with the other 4×4 block $\hat{\mathcal{H}}^{(b)}(\mathbf{k})$, given in Eq. (12b), to form the full $\hat{\mathcal{H}}_{\mathrm{BdG}}$. Also, because of the $\beta_{\mathbf{k}}\omega$ term in Eq. (A2), the expressions for the E_i, in terms of the three coefficients $\{\alpha_{\mathbf{k}},\beta_{\mathbf{k}},\gamma_{\mathbf{k}}\}$, are much more complicated than in the case of $\beta_{\mathbf{k}} = 0$. For brevity we will not present them here.

With the coefficients $\{\alpha_{\mathbf{k}},\beta_{\mathbf{k}},\gamma_{\mathbf{k}}\}$ and E_i defined above, we can now write the final result for $\sigma_H(\omega)$ as follows:

$$\begin{aligned}\sigma_H(\omega) = \sum_{\mathbf{k}} &16i\;\xi_{\mathbf{k}}\,\mathbf{h}\cdot\partial_{k_x}\mathbf{h}\times\partial_{k_y}\mathbf{h}\big\{\widetilde{F}_1(\mathbf{k},\omega) + \big(\xi_{\mathbf{k}}^2 - g_{\mathbf{k}}^2 - |\epsilon_{\mathbf{k}}|^2\big)\widetilde{F}_2(\mathbf{k},\omega)\big\} + 4i\;\xi_{\mathbf{k}}\,(f_{\mathbf{k}}d_{\mathbf{k}}^* - f_{\mathbf{k}}^*d_{\mathbf{k}})\,\Omega_{xy}\,\widetilde{F}_3(\mathbf{k},\omega)\\ &- 8\xi_{\mathbf{k}}\,\mathcal{O}_h(\mathbf{k})\,\widetilde{F}_2(\mathbf{k},\omega),\end{aligned} \tag{A4}$$

where Ω_{xy} was defined in Eq. (25). In Eq. (A4), the three frequency-dependent functions are defined as

$$\widetilde{F}_1(\mathbf{k},\omega) = -\frac{1}{2}\sum_{i=1}^{4}|E_i|\frac{\omega^4 - \omega^2\big(4E_i^2 - \alpha_{\mathbf{k}}\big) + \big(3E_i^4 - \alpha_{\mathbf{k}}E_i^2 + 3\gamma_{\mathbf{k}}\big)}{\prod_{j=1,j\neq i}^{4}(E_j - E_i)\{(E_j - E_i)^2 - \omega^2\}}, \tag{A5a}$$

$$\widetilde{F}_2(\mathbf{k},\omega) = -\frac{1}{2}\sum_{i=1}^{4}|E_i|\frac{-2\omega^2 + \big(9E_i^2 + \alpha_{\mathbf{k}} + \gamma_{\mathbf{k}}/E_i^2\big)}{\prod_{j=1,j\neq i}^{4}(E_j - E_i)\{(E_j - E_i)^2 - \omega^2\}}, \tag{A5b}$$

$$\widetilde{F}_3(\mathbf{k},\omega) = -\frac{1}{2}\sum_{i=1}^{4}\mathrm{sgn}(E_i)\frac{\omega^4 - \omega^2\big(6E_i^2 - \alpha_{\mathbf{k}}\big) + \big(12E_i^4 + 4\gamma_{\mathbf{k}}\big)}{\prod_{j=1,j\neq i}^{4}(E_j - E_i)\{(E_j - E_i)^2 - \omega^2\}}. \tag{A5c}$$

$\widetilde{F}_1$, $\widetilde{F}_2$, and $\widetilde{F}_3$ are connected to the three functions $F_i(\mathbf{k},\omega)$, that we introduced in our perturbative calculations, by

$$\widetilde{F}_1(\mathbf{k},\omega) = \frac{\beta_{\mathbf{k}}}{2}\,F_1(\mathbf{k},\omega) + \mathcal{O}\big(\beta_{\mathbf{k}}^3\big),\quad \widetilde{F}_2(\mathbf{k},\omega) = -\frac{\beta_{\mathbf{k}}}{2\,E_+E_-}\,F_2(\mathbf{k},\omega) + \mathcal{O}\big(\beta_{\mathbf{k}}^3\big),\quad \widetilde{F}_3(\mathbf{k},\omega) = F_3(\mathbf{k},\omega) + \mathcal{O}\big(\beta_{\mathbf{k}}^2\big), \tag{A6}$$

where $E_\pm$ are the two Bogoliubov quasiparticle energies of the zeroth-order Hamiltonian [see Eq. (19)]. From these relations we see that the parameter that controls our perturbative calculation is $\beta_{\mathbf{k}}$ rather than simply $d_{\mathbf{k}}$.

The $\mathcal{O}_h(\mathbf{k})\widetilde{F}_2(\mathbf{k},\omega)$ term in Eq. (A4) contains terms of higher powers, fourth order in $f_{\mathbf{k}}$ and $d_{\mathbf{k}}$, compared with the other terms that are second order in $f_{\mathbf{k}}$ and $d_{\mathbf{k}}$ (ignoring the $f_{\mathbf{k}}$ dependence through the quasiparticle energies $E_\pm$). This is clear from Eq. (A3b), the expression for $\beta_{\mathbf{k}}$, and from

$$\begin{aligned}\mathcal{O}_h(\mathbf{k}) = {}&(|f_{\mathbf{k}}|^2 + |d_{\mathbf{k}}|^2)\,g_{\mathbf{k}}\,\Omega_{xy}\\ &- (|f_{\mathbf{k}}|^2 - |d_{\mathbf{k}}|^2)\big\{\mathrm{Re}[\epsilon_{\mathbf{k}}]\Omega_{xy}^{(1)} + \mathrm{Im}[\epsilon_{\mathbf{k}}]\Omega_{xy}^{(2)}\big\}\\ &+ (f_{\mathbf{k}}d_{\mathbf{k}}^* + f_{\mathbf{k}}^*d_{\mathbf{k}})\big\{\mathrm{Re}[\epsilon_{\mathbf{k}}]\Omega_{xy}^{(2)} - \mathrm{Im}[\epsilon_{\mathbf{k}}]\Omega_{xy}^{(1)}\big\},\end{aligned} \tag{A7}$$

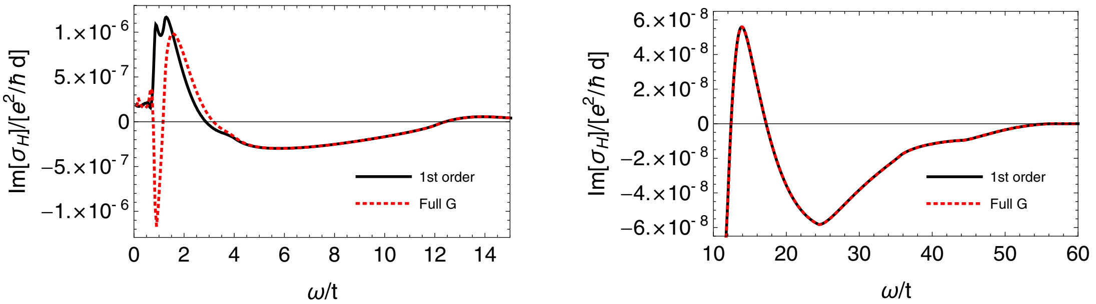

FIG. 7. Comparison between the numerical results for $\mathrm{Im}\,\sigma_H^{(1)}$ (thick black line) and that for $\mathrm{Im}\,\sigma_H$ (dashed red line). Left panel: small $\omega/t \leqslant 14$; right panel: large $\omega/t \geqslant 10$. Notice that the vertical axis scales of the two panels are different. Parameters used are the same as in Fig. 4.

where we have introduced two additional antisymmetrized velocity products $\Omega^{(1)}_{xy}$ and $\Omega^{(2)}_{xy}$, defined as follows:

$$\Omega^{(1)}_{xy} = 2\big\{\partial_{k_x} g_{\mathbf{k}}\ \partial_{k_y}\mathrm{Im}[\epsilon_{\mathbf{k}}] - \partial_{k_x}\mathrm{Im}[\epsilon_{\mathbf{k}}]\ \partial_{k_y} g_{\mathbf{k}}\big\}, \quad \text{(A8a)}$$

$$\Omega^{(2)}_{xy} = 2\big\{\partial_{k_x} g_{\mathbf{k}}\ \partial_{k_y}\mathrm{Re}[\epsilon_{\mathbf{k}}] - \partial_{k_x}\mathrm{Re}[\epsilon_{\mathbf{k}}]\ \partial_{k_y} g_{\mathbf{k}}\big\}. \quad \text{(A8b)}$$

From $\sigma_H(\omega + i\delta)$ in Eq. (A4) we can derive its imaginary part $\mathrm{Im}\,\sigma_H(\omega)$. Then, we can numerically evaluate $\mathrm{Im}\,\sigma_H(\omega)$ and compare the results with our perturbation results for $\mathrm{Im}\,\sigma_H^{(1)}(\omega)$ in the main text. The comparison is given in Fig. 7. We see that the two are quite different for $\omega \lesssim 2\,t$, but they are essentially indistinguishable for $\omega \gtrsim 4t$.

We can also compute $\mathrm{Re}\,\sigma_H(\omega)$ by the Kramers-Kronig transformation and compare the results with $\mathrm{Re}\,\sigma_H^{(1)}$, presented in the main text. This comparison is shown in Fig. 8. Again at $\omega \gtrsim 4t$, the two agree well.

APPENDIX B: DERIVATION OF $\sigma_H^{(1)}$

In order to compute $\sigma_H^{(1)}$, using Eqs. (14) and (23), we introduce the function $\mathcal{F}^{(1)}_{xy}(\mathbf{k}; i\omega_n, i\nu_m)$ such that

$$\pi^{(1)}_{xy}(i\nu_m) - \pi^{(1)}_{yx}(i\nu_m) = T\sum_{\mathbf{k},\omega_n}\mathcal{F}^{(1)}_{xy}(\mathbf{k}; i\omega_n, i\nu_m). \quad \text{(B1)}$$

From the expression for $\pi^{(1)}_{xy}(i\nu_m)$ in Eq. (23), we can write $\mathcal{F}^{(1)}_{xy}$ as follows:

$$\begin{aligned}\mathcal{F}^{(1)}_{xy} \equiv{}& \{\mathrm{Tr}[\hat{v}^x\hat{G}^{(0)}(\mathbf{k}, i\omega_n + i\nu_m)\hat{v}^y\hat{G}^{(1)}(\mathbf{k}, i\omega_n)]\\ &+ \{(0)\leftrightarrow(1)\}\} - \{x \leftrightarrow y\}.\end{aligned} \quad \text{(B2)}$$

This expression contains traces of products of 4 × 4 matrices $\hat{v}^x$, $\hat{G}^{(0)}$, $\hat{v}^y$, and $\hat{G}^{(1)}$. To complete these traces we decompose the 4 × 4 matrices into linear combinations of $\sigma_\alpha\tau_\beta$, where σ_α and τ_α are Pauli matrices for the sublattice and particle-hole Nambu subspaces, respectively. Then,

$$\hat{v}^x = v^x_\alpha\sigma_\alpha\tau_0, \quad \hat{v}^y = v^y_\alpha\sigma_\alpha\tau_0, \quad \text{(B3)}$$

$$\hat{G}^{(0)} = G^{(0)}_{\alpha\beta}\sigma_\alpha\tau_\beta, \quad \hat{G}^{(1)} = G^{(1)}_{\alpha\beta}\sigma_\alpha\tau_\beta. \quad \text{(B4)}$$

We choose the following basis for the above decomposition:

$$\sigma_\alpha \equiv (\sigma_0, \sigma_+, \sigma_-, \sigma_3), \quad \text{(B5)}$$

$$\tau_\alpha \equiv (\tau_0, \tau_+, \tau_-, \tau_3), \quad \text{(B6)}$$

where $\sigma_\pm = (\sigma_1 + i\sigma_2)/\sqrt{2}$ and $\tau_\pm = (\tau_1 + i\tau_2)/\sqrt{2}$. In Eq. (B4), and elsewhere, summations over repeated indices are assumed. In order to extract the coefficients v^x_α, v^y_α, $G^{(0)}_{\alpha\beta}$, and $G^{(1)}_{\alpha\beta}$ it will be convenient to introduce both the conjugate of σ_α, denoted as $\bar{\sigma}_\alpha$, and also the conjugate of α, denoted as $\bar{\alpha}$. Their definitions are

$$\bar{\sigma}_\alpha \equiv [\sigma_\alpha]^\dagger = (\sigma_0, \sigma_-, \sigma_+, \sigma_3) \equiv \sigma_{\bar{\alpha}}. \quad \text{(B7)}$$

Different components of the 4-vectors σ_α and $\bar{\sigma}_\alpha$ satisfy an orthonormal relation: $\mathrm{Tr}\{\sigma_\alpha\bar{\sigma}_\beta\} = 2\delta_{\alpha,\beta}$. Using this relation we can obtain the coefficients in Eq. (B4) as follows:

$$v^x_\alpha = \tfrac{1}{4}\mathrm{Tr}[\hat{v}_x\bar{\sigma}_\alpha\tau_0], \quad v^y_\alpha = \tfrac{1}{4}\mathrm{Tr}[\hat{v}_y\bar{\sigma}_\alpha\tau_0], \quad \text{(B8)}$$

$$G^{(0)}_{\alpha\beta} = \tfrac{1}{4}\mathrm{Tr}[\hat{G}^{(0)}\bar{\sigma}_\alpha\bar{\tau}_\beta], \quad G^{(1)}_{\alpha\beta} = \tfrac{1}{4}\mathrm{Tr}[\hat{G}^{(1)}\bar{\sigma}_\alpha\bar{\tau}_\beta]. \quad \text{(B9)}$$

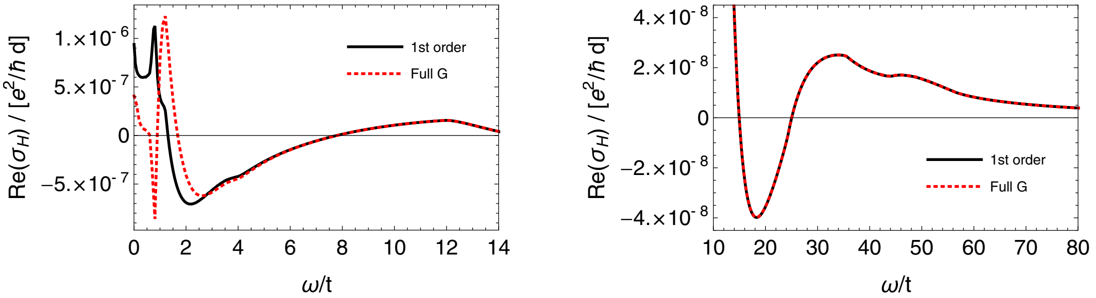

FIG. 8. Comparison between the numerical results for $\mathrm{Re}\,\sigma_H^{(1)}$ (thick black line) and that for $\mathrm{Re}\,\sigma_H$ (dashed red line). Left panel: small $\omega/t \leqslant 14$; right panel: large $\omega/t \geqslant 10$. Note that the vertical axis scales of the two panels are different.

Substituting Eq. (B4) into the expression for $\mathcal{F}_{xy}^{(1)}$ in Eq. (B2) gives

$$\mathcal{F}_{xy}^{(1)} = \big\{ v_\alpha^x G_{\beta\gamma}^{(0)} v_{\alpha'}^y G_{\beta'\gamma'}^{(1)} \, \mathrm{Tr}\,[\sigma_\alpha \sigma_\beta \sigma_{\alpha'} \sigma_{\beta'}] \, \mathrm{Tr}\,[\tau_0 \tau_\gamma \tau_0 \tau_{\gamma'}] + \{(0) \leftrightarrow (1)\} \big\} - \{x \leftrightarrow y\}, \tag{B10}$$

where we have suppressed the arguments of the Green's functions. However, it should be kept in mind that in each of the two Green's function products, the first Green's function should be evaluated at $(\mathbf{k}, i\omega_n + i\nu_m)$, while the second should be evaluated at $(\mathbf{k}, i\omega_n)$. The trace over τ_α Pauli matrix products in Eq. (B10) is trivial: $\mathrm{Tr}\,[\tau_0 \tau_\gamma \tau_0 \tau_{\gamma'}] = 2\,\delta_{\gamma,\gamma'}$. The other trace, $\mathrm{Tr}\,[\sigma_\alpha \sigma_\beta \sigma_{\alpha'} \sigma_{\beta'}]$, is nonzero only for two cases: (1) all four indices $\{\alpha, \beta, \alpha', \beta'\}$ are different from each other; (2) the four indices consist of two identical pairs. However, the latter contribution is even with respect to the interchange $x \leftrightarrow y$ and therefore contributes zero to $\mathcal{F}_{xy}^{(1)}$ after the antisymmetrization $-\{x \leftrightarrow y\}$. Therefore, the only nonzero contribution comes from the case with all four indices different. Because each of the indices $\{\alpha, \beta, \alpha', \beta'\}$ can take four possible values $\{0, +, -, 3\}$ there are $4! = 24$ different terms in total. However, half of them are zero because of the following three identities:

$$G_{+\gamma}^{(0)} G_{-\bar{\gamma}}^{(1)} - G_{-\gamma}^{(0)} G_{+\bar{\gamma}}^{(1)} + \{(0) \leftrightarrow (1)\} = 0, \tag{B11a}$$

$$G_{-\gamma}^{(0)} G_{3\bar{\gamma}}^{(1)} - G_{3\gamma}^{(0)} G_{-\bar{\gamma}}^{(1)} + \{(0) \leftrightarrow (1)\} = 0, \tag{B11b}$$

$$G_{3\gamma}^{(0)} G_{+\bar{\gamma}}^{(1)} - G_{+\gamma}^{(0)} G_{3\bar{\gamma}}^{(1)} + \{(0) \leftrightarrow (1)\} = 0. \tag{B11c}$$

Then, we are left with

$$\begin{aligned} \mathcal{F}_{xy}^{(1)} = 8\big\{ &\big\{ v_-^x v_3^y - v_3^x v_-^y \big\} \big\{ G_{0\gamma}^{(0)} G_{+\bar{\gamma}}^{(1)} - G_{+\gamma}^{(0)} G_{0\bar{\gamma}}^{(1)} + \{(0) \leftrightarrow (1)\} \big\} + \big\{ v_3^x v_+^y - v_+^x v_3^y \big\} \big\{ G_{0\gamma}^{(0)} G_{-\bar{\gamma}}^{(1)} - G_{-\gamma}^{(0)} G_{0\bar{\gamma}}^{(1)} + \{(0) \leftrightarrow (1)\} \big\} \\ &+ \big\{ v_+^x v_-^y - v_-^x v_+^y \big\} \big\{ G_{0\gamma}^{(0)} G_{3\bar{\gamma}}^{(1)} - G_{3\gamma}^{(0)} G_{0\bar{\gamma}}^{(1)} + \{(0) \leftrightarrow (1)\} \big\} \big\}. \end{aligned} \tag{B12}$$

In obtaining this equation we have used the trace identity $\mathrm{Tr}[\sigma^0 \sigma^+ \sigma^- \sigma^3] = 2$ as well as its permutations.

Next we need to complete the the Matsubara summation $T \sum_{\omega_n}$ in Eq. (B1). This can be done for each of the three terms in Eq. (B12). The derivations are quite lengthy, and we do not present them here. The final results are

$$T \sum_n G_{0\gamma}^{(0)} G_{+\bar{\gamma}}^{(1)} - G_{+\gamma}^{(0)} G_{0\bar{\gamma}}^{(1)} + \{(0) \leftrightarrow (1)\} = 4i \, \{ f_\mathbf{k} d_\mathbf{k}^* - f_\mathbf{k}^* d_\mathbf{k} \} \, \xi_\mathbf{k} \, g_\mathbf{k} \, \sqrt{2} \epsilon_\mathbf{k} \, S_\mathbf{k}(i\nu_m), \tag{B13a}$$

$$T \sum_n G_{0\gamma}^{(0)} G_{-\bar{\gamma}}^{(1)} - G_{-\gamma}^{(0)} G_{0\bar{\gamma}}^{(1)} + \{(0) \leftrightarrow (1)\} = 4i \, \{ f_\mathbf{k} d_\mathbf{k}^* - f_\mathbf{k}^* d_\mathbf{k} \} \, \xi_\mathbf{k} \, g_\mathbf{k} \, \sqrt{2} \epsilon_\mathbf{k}^* \, S_\mathbf{k}(i\nu_m), \tag{B13b}$$

$$T \sum_n G_{0\gamma}^{(0)} G_{3\bar{\gamma}}^{(1)} - G_{3\gamma}^{(0)} G_{0\bar{\gamma}}^{(1)} + \{(0) \leftrightarrow (1)\} = 4i \, \{ f_\mathbf{k} d_\mathbf{k}^* - f_\mathbf{k}^* d_\mathbf{k} \} \, \xi_\mathbf{k} \, g_\mathbf{k} \, 2g_\mathbf{k} \, S_\mathbf{k}(i\nu_m) - 2i \, \{ f_\mathbf{k} d_\mathbf{k}^* - f_\mathbf{k}^* d_\mathbf{k} \} \, \xi_\mathbf{k} \, T_\mathbf{k}(i\nu_m). \tag{B13c}$$

For brevity, we have introduced two frequency-dependent functions $S_\mathbf{k}(i\nu_m)$ and $T_\mathbf{k}(i\nu_m)$, which are defined as

$$S_\mathbf{k}(i\nu_m) \approx M_1 - \big(\xi_\mathbf{k}^2 - g_\mathbf{k}^2 - |\epsilon_\mathbf{k}|^2\big) M_2, \tag{B14}$$

$$T_\mathbf{k}(i\nu_m) \approx \frac{-i\nu_m}{2E_+ E_- (E_+ + E_-)\{(E_+ + E_-)^2 + \nu_m^2\}}, \tag{B15}$$

where the $\approx$ sign means only terms of leading order in $f_\mathbf{k}$ and $d_\mathbf{k}$ have been kept. M_1 and M_2 are given by

$$M_1 = -i\nu_m \left\{ \frac{C_{++}}{4E_+^2 + \nu_m^2} + \frac{C_{--}}{4E_-^2 + \nu_m^2} + \frac{C_{+-}}{(E_+ + E_-)^2 + \nu_m^2} + \frac{C'_{+-}}{\{(E_+ + E_-)^2 + \nu_m^2\}^2} \right\}, \tag{B16a}$$

$$M_2 = \frac{-i\nu_m}{E_+ E_-} \left\{ \frac{D_{++}}{4E_+^2 + \nu_m^2} + \frac{D_{--}}{4E_-^2 + \nu_m^2} + \frac{D_{+-}}{(E_+ + E_-)^2 + \nu_m^2} + \frac{D'_{+-}}{\{(E_+ + E_-)^2 + \nu_m^2\}^2} \right\}, \tag{B16b}$$

where C_{++}, C_{--}, C_{+-}, C'_{+-}, D_{++}, D_{--}, D_{+-}, and D'_{+-} are eight ν_m independent coefficients. The expressions for C_{++}, C_{--}, C_{+-}, D_{++}, D_{--}, and D_{+-} were given in Eqs. (29a)–(29e). The other two coefficients are as follows:

$$C'_{+-} = D'_{+-} = \frac{-2}{(E_+ + E_-)(E_+ - E_-)^2}. \tag{B17}$$

Notice that both the C'_{+-} term in Eq. (B16a) and the D'_{+-} term in Eq. (B16b) have a second-order pole at $\nu_m = \pm i(E_+ + E_-)$ on the complex ν_m plane, while all other terms have first-order poles. The second-order poles appear only in the perturbative calculation but not in the full $\hat{G}$ calculation. Numerically, we found that the second-order pole contributions to $\sigma_H^{(1)}$ from Eqs. (B16a) and (B16b) are negligible at $\omega \gg \alpha$, where α is the SOC coupling strength. Hence, we will ignore them hereafter. Performing a Wick rotation $i\nu_m \to \omega + i\delta$, we see that $S_\mathbf{k}(\omega)/\omega$ and $T_\mathbf{k}(\omega)/\omega$ are given by Eqs. (26) and (27).

Now, inserting the results from Eqs. (B13a)–(B13c) into the expression for $\mathcal{F}^{(1)}_{xy}$ in Eq. (B12) we obtain

$$T\sum_n \mathcal{F}^{(1)}_{xy} = 64i\,\{f_{\mathbf{k}}d^*_{\mathbf{k}} - f^*_{\mathbf{k}}d_{\mathbf{k}}\}\,\xi_{\mathbf{k}}\,g_{\mathbf{k}}\,S_{\mathbf{k}}(i\nu_m)\,\mathbf{h}\cdot\partial_{k_x}\mathbf{h} \times\partial_{k_y}\mathbf{h} + 8\,\{f_{\mathbf{k}}d^*_{\mathbf{k}} - f^*_{\mathbf{k}}d_{\mathbf{k}}\}\,\xi_{\mathbf{k}}\,T_{\mathbf{k}}(i\nu_m)\Omega_{xy}, \tag{B18}$$

where we have used

$$\begin{aligned}\mathbf{h}\cdot\partial_{k_x}\mathbf{h}\times\partial_{k_y}\mathbf{h} &= \left[v^x_- v^y_3 - v^x_3 v^y_-\right]\epsilon_{\mathbf{k}}/\sqrt{2} + \left[v^x_3 v^y_+ - v^x_+ v^y_3\right]\epsilon^*_{\mathbf{k}}/\sqrt{2}\\ &\quad + \left[v^x_+ v^y_- - v^x_- v^y_+\right]g_{\mathbf{k}},\end{aligned} \tag{B19}$$

and also introduced a notation Ω_{xy} for the following antisymmetrized velocity factor:

$$\Omega_{xy} \equiv -2i\,[v^x_+ v^y_- - v^x_- v^y_+] = -i[\partial_{k_x}\epsilon_{\mathbf{k}}\partial_{k_y}\epsilon^*_{\mathbf{k}} - \partial_{k_x}\epsilon^*_{\mathbf{k}}\partial_{k_y}\epsilon_{\mathbf{k}}]. \tag{B20}$$

With these compact notations one can substitute $T\sum_n \mathcal{F}^{(1)}_{xy}$ from Eq. (B18) back into Eq. (B1) and obtain the final expression for the Hall conductivity as a function of frequency given in Eq. (24).

APPENDIX C: ASYMPTOTIC RESULT FOR LARGE ω AND SUM RULES

In this Appendix, we compute $\langle[\hat{J}_x,\hat{J}_y]\rangle$ on the right-hand side of Eq. (33) for the BdG Hamiltonian $\hat{\mathcal{H}}^{(a)}(\mathbf{k})$ in Eq. (12a) up to first order in $\hat{\mathcal{H}}'$. Denote the basis of the Hamiltonian $\hat{\mathcal{H}}^{(a)}(\mathbf{k})$ from Eq. (12a) as $\Psi \equiv (\Psi_1,\Psi_2,\Psi_3,\Psi_4)^T$. Then, the current operator can be written as $\hat{J}_i = \sum_{\mathbf{k}}\sum_{\alpha\beta}\Psi^\dagger_\alpha(\mathbf{k})\,v^i_{\alpha\beta}\,\Psi_\beta(\mathbf{k})$, with $i = \{x,y\}$. The velocity operator matrix $v^i_{\alpha\beta}$ is given in Eq. (22). Using the fact that the equal-time expectation value $\langle\Psi^\dagger_\alpha\Psi_\beta\rangle = T\sum_n \hat{G}_{\beta\alpha}(\mathbf{k},i\omega_n)$, we obtain

$$\langle[\hat{J}_x,\hat{J}_y]\rangle = \sum_{\mathbf{k}} T\sum_n\{A\{G_{11} - G_{22} + G_{33} - G_{44}\} + B\{G_{21} + G_{43}\} - B^*\{G_{12} + G_{34}\}\}, \tag{C1}$$

with A and B given by

$$A = \partial_{k_x}\epsilon_{\mathbf{k}}\partial_{k_y}\epsilon^*_{\mathbf{k}} - \partial_{k_x}\epsilon^*_{\mathbf{k}}\partial_{k_y}\epsilon_{\mathbf{k}}, \tag{C2a}$$

$$B = 2(\partial_{k_x}g_{\mathbf{k}}\partial_{k_y}\epsilon_{\mathbf{k}} - \partial_{k_x}\epsilon_{\mathbf{k}}\partial_{k_y}g_{\mathbf{k}}). \tag{C2b}$$

On the right-hand side of Eq. (C1), all Green's function matix elements are evaluated at $(\mathbf{k},i\omega_n)$.

In Eq. (C1), if we use the zeroth-order result $G^{(0)}_{\alpha\beta}$ for all the Green's function matrix elements, then we obtain $\langle[\hat{J}_x,\hat{J}_y]\rangle^{(0)} = 0$. This is consistent with Eq. (33) and the fact that $\sigma^{(0)}_H(\omega) \equiv 0$.

The nonzero $\langle[\hat{J}_x,\hat{J}_y]\rangle$ comes from the next-order contribution: $\langle[\hat{J}_x,\hat{J}_y]\rangle^{(1)}$. Substituting the matrix elements of the first-order Green's function $\hat{G}^{(1)} \equiv \hat{G}^{(0)}\hat{\mathcal{H}}'\hat{G}^{(0)}$ into Eq. (C1) and completing the Matsubara summation

$$\langle[J_x,J_y]\rangle^{(1)} = i\sum_{\mathbf{k}}\frac{-2i\,\xi_{\mathbf{k}}(f_{\mathbf{k}}d^*_{\mathbf{k}} - f^*_{\mathbf{k}}d_{\mathbf{k}})}{E_+E_-(E_+ + E_-)} \times\left\{\Omega_{xy} + 8i\,\frac{g_{\mathbf{k}}\,\mathbf{h}\cdot\partial_{k_x}\mathbf{h}\times\partial_{k_y}\mathbf{h}}{(E_+ + E_-)^2}\right\}, \tag{C3}$$

where Ω_{xy} is defined in Eq. (25). The remaining $\mathbf{k}$ summation in Eq. (C3) can be evaluated numerically and the final result is $\langle[J_x,J_y]\rangle^{(1)} \approx -i\,2.2\times 10^{-5}t^2\,e^2/(\hbar\,d)$. Then, Eq. (33) becomes

$$\frac{\sigma^{(1)}_H(\omega\to\infty)}{e^2/\hbar\,d} = \frac{2.2\times 10^{-5}}{(\omega/t)^2} + O\left(\frac{1}{(\omega/t)^4}\right). \tag{C4}$$

It is also possible to perform the integral in Eq. (35) analytically using $\mathrm{Im}\,\sigma^{(1)}_H(\omega)$ from Eq. (30). The result is identical to $-i$ times Eq. (C3). Similarly, the integral of Eq. (34) can be performed analytically using Eqs. (24)–(28c). The zero result follows from the analytic structure of the $F_i(\mathbf{k},\omega)$ in Eqs. (28a)–(28c). We also numerically evaluate the two sides of Eqs. (34) and (35) using the data from Figs. 4 and 5 and confirm that Eqs. (34) and (35) are well satisfied.

APPENDIX D: ESTIMATION OF THE NN HOPPING t

We plot the two normal-state energy band dispersions along high-symmetry directions in Fig. 9. From the dispersions along A − L − H − A, the corresponding bandwidth in the $k_z = 0$ plane is $W \approx 14t$. We can fit this to the first-principles calculation results from Ref. [53]. From the Supplemental Material Fig. S1(b) of Ref. [53], we estimate that the bandwidth of the dispersions along A − L − H − A is $W \approx 0.5$ eV. Therefore, as an estimation, $14t \approx 0.5$ eV $\Rightarrow t \approx 36$ meV.

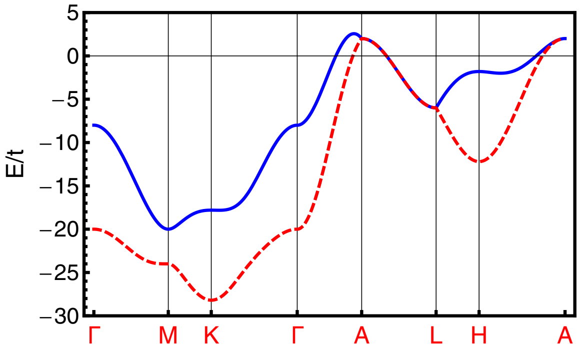

FIG. 9. Normal-state energy dispersions along high-symmetry directions of the hexagonal Brillouin zone at $k_z = \pi$. The two energy band dispersions are $E^{(n)}_\pm(\mathbf{k}) = \xi_{\mathbf{k}} \pm \sqrt{g^2_{\mathbf{k}} + |\epsilon_{\mathbf{k}}|^2}$, with $E^{(n)}_+$ plotted in full blue line and $E^{(n)}_-$ in the dashed red line. The two bands are degenerate along the symmetry axis A − L because $\epsilon_{\mathbf{k}} = 0$ at $k_z = \pi$ and the SOC vanishes along these directions as well.

We note that the bands along $\Gamma - \mathrm{M} - \mathrm{K} - \Gamma$ in Fig. 9 are far below the Fermi energy, which is inconsistent with the realistic first-principles calculation result in Ref. [53]. This is due to the oversimplification of our model which consists of only two bands resulting from the ABAB stacking. Due to this oversimplification, the dispersions along $\Gamma - \mathrm{M} - \mathrm{K} - \Gamma$ are not realistic. In order to estimate how these unrealistic dispersions affect our calculations of θ_K, we have recomputed θ_K by excluding all $\mathbf{k}$ points that satisfy $E_{\pm}^{(n)}(\mathbf{k}) \leqslant E_{-}^{(n)}(\mathbf{k} = H)$, where $E_{-}^{(n)}(\mathbf{k} = H)$ is the band bottom of the dispersions along $\mathrm{A} - \mathrm{L} - \mathrm{H} - \mathrm{A}$ in Fig. 9. The result is similar to the value obtained in the main text without this truncation. In other words, the unrealistic dispersions along $\Gamma - \mathrm{M} - \mathrm{K} - \Gamma$ do not significantly change our conclusion for θ_K. This is because the main contribution to σ_H comes from k_z values closer to $k_z = \pi$ and not from the region near $k_z = 0$ in the BZ.

[1] C. Kallin and J. Berlinsky, Rep. Prog. Phys. **79**, 054502 (2016).
[2] A. Kapitulnik, J. Xia, E. Schemm, and A. Palevski, New J. Phys. **11**, 055060 (2009).
[3] P. N. Argyres, Phys. Rev. **97**, 334 (1955).
[4] J. Xia, Y. Maeno, P. T. Beyersdorf, M. M. Fejer, and A. Kapitulnik, Phys. Rev. Lett. **97**, 167002 (2006).
[5] E. R. Schemm, W. J. Gannon, C. M. Wishne, W. P. Halperin, and A. Kapitulnik, Science **345**, 190 (2014).
[6] E. R. Schemm, R. E. Baumbach, P. H. Tobash, F. Ronning, E. D. Bauer, and A. Kapitulnik, Phys. Rev. B **91**, 140506 (2015).
[7] E. Levenson-Falk, E. Schemm, M. Maple, and A. Kapitulnik, arXiv:1609.07535.
[8] X. Gong, M. Kargarian, A. Stern, D. Yue, H. Zhou, X. Jin, V. M. Galitski, V. M. Yakovenko, and J. Xia, Sci. Adv. **3**, e1602579 (2017).
[9] C. Kallin and A. J. Berlinsky, J. Phys.: Condens. Matter **21**, 164210 (2009).
[10] A. P. Mackenzie, T. Scaffidi, C. W. Hicks, and Y. Maeno, Quantum Mater. **2**, 40 (2017).
[11] J. Sauls, Adv. Phys. **43**, 113 (1994).
[12] M. Norman, Phys. C (Amsterdam) **194**, 203 (1992).
[13] N. Read and D. Green, Phys. Rev. B **61**, 10267 (2000).
[14] R. Roy and C. Kallin, Phys. Rev. B **77**, 174513 (2008).
[15] R. M. Lutchyn, P. Nagornykh, and V. M. Yakovenko, Phys. Rev. B **80**, 104508 (2009).
[16] J. Goryo, Phys. Rev. B **78**, 060501 (2008).
[17] E. J. König and A. Levchenko, Phys. Rev. Lett. **118**, 027001 (2017).
[18] S. K. Yip and J. A. Sauls, J. Low Temp. Phys. **86**, 257 (1992).
[19] E. Taylor and C. Kallin, Phys. Rev. Lett. **108**, 157001 (2012).
[20] E. Taylor and C. Kallin, J. Phys.: Conf. Ser. **449**, 012036 (2013).
[21] K. I. Wysokiński, J. F. Annett, and B. L. Györffy, Phys. Rev. Lett. **108**, 077004 (2012).
[22] M. Gradhand, K. I. Wysokinski, J. F. Annett, and B. L. Györffy, Phys. Rev. B **88**, 094504 (2013).
[23] V. P. Mineev, Phys. Rev. B **89**, 134519 (2014).
[24] W. Huang, S. Lederer, E. Taylor, and C. Kallin, Phys. Rev. B **91**, 094507 (2015).
[25] Y. Tada, W. Nie, and M. Oshikawa, Phys. Rev. Lett. **114**, 195301 (2015).
[26] G. E. Volovik, JETP Lett. **100**, 742 (2015).
[27] R. A. Fisher, S. Kim, B. F. Woodfield, N. E. Phillips, L. Taillefer, K. Hasselbach, J. Flouquet, A. L. Giorgi, and J. L. Smith, Phys. Rev. Lett. **62**, 1411 (1989).
[28] G. Bruls, D. Weber, B. Wolf, P. Thalmeier, B. Lüthi, A. de Visser, and A. Menovsky, Phys. Rev. Lett. **65**, 2294 (1990).
[29] S. Adenwalla, S. W. Lin, Q. Z. Ran, Z. Zhao, J. B. Ketterson, J. A. Sauls, L. Taillefer, D. G. Hinks, M. Levy, and B. K. Sarma, Phys. Rev. Lett. **65**, 2298 (1990).
[30] R. Joynt and L. Taillefer, Rev. Mod. Phys. **74**, 235 (2002).
[31] J. Gouchi, A. Sumiyama, A. Yamaguchi, G. Motoyama, N. Kimura, E. Yamamoto, Y. Haga, and Y. Onuki, J. Phys.: Conf. Ser. **592**, 012066 (2015).
[32] S. M. Hayden, L. Taillefer, C. Vettier, and J. Flouquet, Phys. Rev. B **46**, 8675 (1992).
[33] B. Lussier, B. Ellman, and L. Taillefer, Phys. Rev. B **53**, 5145 (1996).
[34] The splitting of these two transitions has been attributed to very weak antiferromagnetic order (which we ignore in our analysis). See, for example, Ref. [11].
[35] Y. Yanase, Phys. Rev. B **94**, 174502 (2016).
[36] Note that the crystal structure of UPt_3 is far from the ideal hcp structure. U atoms in each UPt_3 layer form a hexagonal lattice with a Pt atom between each nearest-neighbor pair of U atoms, which means that the lattice of U atoms in each layer is greatly expanded compared, for example, to uranium metal. By comparison, the $\mathrm{U} - \mathrm{U}$ nearest-neighbor distance for neighboring layers is much shorter, only 0.72 of the intralayer $\mathrm{U} - \mathrm{U}$ distance. The c-axis distance is also rather short, with c/a ratio of only 0.85, compared to the ideal hcp ratio of 1.633.
[37] G. J. McMullan, P. M. C. Rourke, M. R. Norman, A. D. Huxley, N. Doiron-Leyraud, J. Flouquet, G. G. Lonzarich, A. McCollam, and S. R. Julian, New J. Phys. **10**, 053029 (2008).
[38] M. H. Fischer, F. Loder, and M. Sigrist, Phys. Rev. B **84**, 184533 (2011).
[39] D. Maruyama, M. Sigrist, and Y. Yanase, J. Phys. Soc. Jpn. **81**, 034702 (2012).
[40] H. Tou, Y. Kitaoka, K. Ishida, K. Asayama, N. Kimura, Y. Onuki, E. Yamamoto, Y. Haga, and K. Maezawa, Phys. Rev. Lett. **80**, 3129 (1998).
[41] M. Sigrist and K. Ueda, Rev. Mod. Phys. **63**, 239 (1991).
[42] E. I. Blount, Phys. Rev. B **32**, 2935 (1985).
[43] M. R. Norman, Phys. Rev. B **52**, 15093 (1995).
[44] T. Micklitz and M. R. Norman, Phys. Rev. B **80**, 100506 (2009).
[45] S. Kobayashi, Y. Yanase, and M. Sato, Phys. Rev. B **94**, 134512 (2016).
[46] T. Micklitz and M. R. Norman, Phys. Rev. B **95**, 024508 (2017).
[47] T. Micklitz and M. R. Norman, Phys. Rev. Lett. **118**, 207001 (2017).
[48] G. D. Mahan, *Many-Particle Physics* (Plenum, New York, 1990).
[49] B. S. Shastry, B. I. Shraiman, and R. R. P. Singh, Phys. Rev. Lett. **70**, 2004 (1993).
[50] E. Lange and G. Kotliar, Phys. Rev. Lett. **82**, 1317 (1999).
[51] H. D. Drew and P. Coleman, Phys. Rev. Lett. **78**, 1572 (1997).
[52] P. E. Sulewski, A. J. Sievers, M. B. Maple, M. S. Torikachvili, J. L. Smith, and Z. Fisk, Phys. Rev. B **38**, 5338 (1988).

[53] T. Nomoto and H. Ikeda, Phys. Rev. Lett. **117**, 217002 (2016).

[54] J. Schoenes and J. Franse, Phys. B+C (Amsterdam) **130**, 69 (1985).

[55] M. Dressel, N. Kasper, K. Petukhov, B. Gorshunov, G. Grüner, M. Huth, and H. Adrian, Phys. Rev. Lett. **88**, 186404 (2002).

[56] F. Marabelli, G. Travaglini, P. Wachter, and J. Franse, Solid State Commun. **59**, 381 (1986).

[57] G. Goll, H. v. Löhneysen, I. K. Yanson, and L. Taillefer, Phys. Rev. Lett. **70**, 2008 (1993).

[58] G. Goll, C. Bruder, and H. v. Löhneysen, Phys. Rev. B **52**, 6801 (1995).

[59] R. Joynt and W.-C. Wu, Sci. Rep. **7**, 12968 (2017).

[60] C. S. Wang, M. R. Norman, R. C. Albers, A. M. Boring, W. E. Pickett, H. Krakauer, and N. E. Christensen, Phys. Rev. B **35**, 7260 (1987).